analytica

MDPI

Article

Physicochemical Assessment of Selected Conductive Polymers for Probable Mercury Remediation in Wastewater—Experimental and DFT Approach

Sesona Macanda [1,2], Hassan Shoyiga [2,*], Adeniyi Ogunlaja [3], Uliana Pinaeva [4], Sizwe Zamisa [5] and Nobathembu Faleni [2,*]

[1] Department of Chemical and Physical Sciences, Faculty of Natural Sciences, Walter Sisulu University, Nelson Mandela Drive, P/Bag X1, Mthatha 5117, South Africa
[2] Department of Applied Science, Faculty of Natural Sciences, Walter Sisulu University, Old King William Town Road, Potsdam Site, East London 5200, South Africa
[3] Department of Chemistry, Nelson Mandela University, Gqeberha 6070, South Africa
[4] Joint Institute for Nuclear Research, Joliot-Curie St. 6, Dubna 141980, Moscow Region, Russia
[5] School of Chemistry and Physics, University of KwaZulu-Natal, Private Bag X54001, Durban 4001, South Africa
* Correspondence: hshoyiga@wsu.ac.za (H.S.); nfaleni@wsu.ac.za (N.F.)

Abstract

Mercury contamination in aquatic environments poses significant risks to ecosystems and human health, underscoring the need for effective remediation technologies. This research examines the physicochemical properties of the synthesised polymer materials, and DFT calculations were used as an initial step for material development to validate our experimental outcomes for the prepared polymers: polyaniline (PANI), polyethersulfone (PES), and polyamidoamine (PAMAM). Furthermore, DFT studies were used to elucidate structure–property relationships in polymers, serving as performance predictors for mercury adsorption and selectivity, as well as for their applicability in electronic sensors. The characterisation techniques indicated the high functional group densities of PAMAM dendrimers for effective chelation, while the semi-crystalline structure of PANI improves metal binding. DFT calculations reveal that PAMAM exhibits the smallest HOMO–LUMO energy gap, indicating a high reactivity towards mercury ions. Binding energies indicate that PAMAM forms the most stable single-ion complex; PAM1Hg (0.242 eV, 23.37 kJ mol^{-1}), whereas PES exhibits enhanced interaction at elevated mercury concentrations, resulting in stable multi-Hg complexes, PES3Hg (0.136 eV, 13.13 kJ/mol). The findings indicate that nitrogen-rich functional groups and aromatic systems play a crucial role in mercury binding, highlighting the promise of conductive polymers for creating effective adsorbents aimed at mercury remediation in industrial wastewater.

Keywords: mercury remediation; DFT; heavy metals; conductive polymers; binding energy; adsorption

Academic Editor: Marcello Locatelli

Received: 21 June 2026
Revised: 24 July 2026
Accepted: 6 August 2026
Published: 13 August 2026

1. Introduction

There has been a corresponding increase in the concentration of heavy metals found in wastewater due to the expansion of industry and human activities [1]. The introduction of wastewater laden with heavy metals into the environment adversely affects both human populations and the ecosystems [2]. Heavy metals exhibit non-biodegradable properties

and are recognised for their carcinogenic potential [3]. Consequently, elevated concentrations of these metals in water can lead to significant health issues for organisms [4]. The heavy metals that are most commonly recognised include lead (Pb), zinc (Zn), mercury (Hg), nickel (Ni), cadmium (Cd), copper (Cu), chromium (Cr), and arsenic (As). Even in trace amounts, these heavy metals pose significant health and environmental risks [5]. Hg is recognised as one of the most toxic metals and is widely used across various industries, including pesticides, chlorine–alkali chemistry, batteries, and electronic devices. Mercury (II) (Hg^{2+}) ions in water exhibit significant reactivity and pose a considerable risk to human health and ecological systems [3]. Methylation of Hg^{2+} ions occurs readily, leading to significant toxicity even at low doses (1.6 μg kg^{-1}) [4]. The US Environmental Protection Agency has established a mercury concentration limit of 0.01 mg L^{-1} for wastewater discharge [5], while in China, the limit is set at 0.05 mg L^{-1} [6]. In South Africa, regulatory bodies have established strict discharge restrictions because of the substance's bio-accumulative properties and toxicity, even at minimal concentrations [7]. Typically, in South Africa, the South African Bureau of Standards (SANS 241) sets a limit of $\leq$0.006 mg L^{-1} for mercury concentration, and the Department of Water and Sanitation (RSA) sets a limit of <0.002 mg L^{-1} for mercury concentration in effluent discharge. Consequently, it is crucial to develop cost-effective methods for the effective removal of Hg^{2+} ions from water bodies to ensure public health safety [7,8].

Among the diverse array of water treatment technologies developed, adsorption stands out as one of the most promising methods. Conventional adsorbents such as clay [9,10], activated carbon [11], zeolite [12], and waste biomass [13] have been investigated for their efficacy in mercury removal. Furthermore, innovative chemically engineered materials such as layered double hydroxides [14], metal–organic frameworks (MOFs) [15], and MoS_2 nanosheets [16], as well as polyaniline and polypyrrole composites [17,18], have been explored and have shown promising results. Nonetheless, many of these adsorbents exhibit limited adsorption capacity, inadequate selectivity, and insufficient regeneration capabilities. Moreover, these adsorbents require extreme pH conditions and intricate preparation processes, are costly, and are therefore impractical for their intended applications. Removing Hg^{2+} ions to meet the established safety standards presents a significant challenge. Therefore, it is essential to develop innovative adsorption materials for the removal of Hg^{2+} ions. Historically, polymers have been categorised as non-conductive materials, due to their stable molecular structure characterised by covalent bonds within a saturated carbon framework [19]. However, the discovery and development of conductive polymers have sparked a growing interest in the domain of polymeric conductive materials.

Conducting polymers possess a significant quantity of delocalised π-electrons, which facilitate their ability to conduct electricity and engage in electrostatic interactions with other charged molecules [9]. These characteristics are crucial for the effective removal of contaminants in wastewater. Polyaniline (PANI) stands out as a highly attractive material for the removal of mercury from wastewater, owing to its distinctive characteristics, including robust electrical conductivity, impressive electrochemical performance, significant chemical stability, exceptional redox behaviour, mechanical flexibility, and affordability [20,21]. Recent studies by Ganachari et al. [22] and Mustafa et al. [9] demonstrate enhanced heavy-metal removal using PANI-based composites. The spectroscopic and morphological analyses confirm their granular, porous structure, which facilitates rapid membrane integration and Hg^{2+} uptake.

This study examines the synthesis, characterisation, and comparative physicochemical properties of three conductive polymers: polyaniline (PANI), polyethersulfone (PES), and polyamidoamine (PAMAM). It explores how these properties position them as po-

tential adsorbents for mercury remediation in wastewater. Polyethersulfone (PES) stands out as a highly promising adsorbent material within the sulfone polymer family, particularly among amorphous polymers, due to its exceptional mechanical, chemical, and thermal strength [2,14]. Polyamidoamine (PAMAM) dendrimer, in contrast, is a hyperbranched polymer characterised by internal cavities, a large number of terminal functional groups, a highly cross-linked structure, and a significant adsorption capacity that increases with generation. This makes it an attractive option for mercury removal in wastewater, as mercury is drawn to the nitrogen atom, facilitating easy bonding and the formation of stable complexes [15,16]. Thanks to advancements in computer technology, it is now possible to analyse the adsorption mechanism of heavy metal ions on polymeric materials at the molecular level through simulations. Additionally, in light of the environmental issues associated with mercury and its organic derivatives, numerous theoretical [23,24] and experimental [25] investigations have been conducted to remove these species *via* adsorption. Various matrices, including graphitic carbon nitride, vanillin, cellulose xanthate, sulphur-containing biomass composites, and carbon nanotubes, were utilised for DFT studies [23]. Bihain et al. [26] conducted a comparative study at the theoretical level using wB97X-D/6–31 + G(d,p)/LANL2DZ, examining the matrices cellulose xanthate (XC), graphitic carbon nitride (g-C_3N_4), and modified vanillin monomer (VN) to determine the most effective adsorbent matrix for the organic species methylmercury (CH_3Hg^+) [26]. The observed results confirmed that the most effective matrix for interaction with CH_3Hg^+ was VN, due to the presence of a shift base, with $\Delta E_{bind} = -1.15$ kcal mol^{-1} and bond lengths ranging from 2.56 to 2.66 Å. Similarly, studies by Lan et al. [27] demonstrated the use of heteroatom-doped carbon nanotubes (CNTs) and DFT calculations for the adsorption of various metal ions. The authors explore various doping methods for nanotubes, including heteroatom doping with oxygen, boron, boron–nitrogen, nitrogen, and sulphur, as well as undoped nanotubes. The sequence of binding energy for Hg^{2+} with CNTs was observed as N-CNT > O-CNT > CNT > B-N-CNT > B-CNT > S-CNT, suggesting that incorporating dopants like nitrogen and oxygen enhances the adsorption affinity of Hg^{2+} on CNTs. The use of DFT is valuable for exploring molecular-level interactions between heavy metal ions and polymer materials, enhancing understanding of these intricate interactions during adsorption.

Although there is a large body of literature on individual polymer adsorbents for mercury removal, a systematic and comprehensive comparison of three polymer classes with different structures, namely a linear π-conjugated polymer (PANI), a thermoplastic engineering polymer (PES) and a hyperbranched dendrimer (PAMAM), under homogeneous DFT conditions and their experimental physicochemical characterisation has not been reported before. Previous computational studies on mercury adsorption have been mostly carried out on carbon-based adsorbents (graphitic carbon nitride, carbon nanotubes, and graphene oxide), using different DFT approaches, making it difficult to make a direct comparison. Moreover, the use of several Hg^{2+} loading cases (1 Hg vs. 3 Hg) to probe the site saturation behaviour is a methodological breakthrough above single-ion DFT research. The simultaneous presence of three different binding mechanisms, i.e., π-conjugated (PANI), sulfone-mediated soft coordination (PES) and amine/amide chelation (PAMAM) in a unified comparative DFT framework, allows for a structure-binding-mechanism analysis that leads to informed design of advanced polymer-based adsorbents for mercury remediation. Thus, the present investigation: (1) synthesises and characterises PANI, PES and PAMAM by a comprehensive multi-technique analysis (SEM/EDX, XRD, UV–Vis, FTIR); (2) performs DFT calculations at B3LYP/LANL2DZ/6-311G(d,p). This technique offers a fundamental understanding of systematic polymer design while simultaneously

acknowledging the technical constraints, such as shape, solvation, and scalability, that are present in practical mercury remediation settings.

2. Materials and Methods

2.1. Materials

Aniline hydrochloride, ammonium peroxydisulfate ($(NH_4)_2S_2O_8$), hydrochloric acid (HCl), sodium hydroxide (NaOH), bisphenol A, bis(4-fluorophenyl) sulfone (BFS), ethylenediamine (EDA), methyl acrylate, methanol, dimethyl sulfoxide (DMSO), and potassium carbonate were acquired from Sigma-Aldrich, Johannesburg, South Africa. All reagents were of analytical grade and used as received without further purification. All solutions were formulated using deionised (DI) water.

2.2. Synthesis of PANI

To synthesise PANI, a modified method reported by Mokole et al. [28] was employed. A measurement of 20 mL of aniline monomer was combined with 200 mL of 1 M HCl, and the mixture was stirred continuously to ensure complete protonation of the aniline. Subsequently, 2.13 g of aniline blue was added to the mixture as a dopant and potential morphology modifier. After achieving a homogeneous solution, ammonium persulfate (APS) was introduced dropwise as an oxidising agent in a 1:1 molar ratio with respect to aniline. The reaction mixture was subsequently stirred continuously in an ice bath maintained at 0–5 °C to regulate the polymerisation rate and preserve structural integrity. The polymerisation process was allowed to continue for 4–6 h, during which the solution turned dark green, indicating the formation of the emeraldine salt form of PANI. The precipitate obtained was filtered, then washed with deionised water and ethanol to remove any unreacted monomers and by-products, and finally dried under vacuum at room temperature. The chemical reaction of the process is depicted in Scheme 1, whereas Figure 1 provides a schematic diagram of the synthesis procedure.

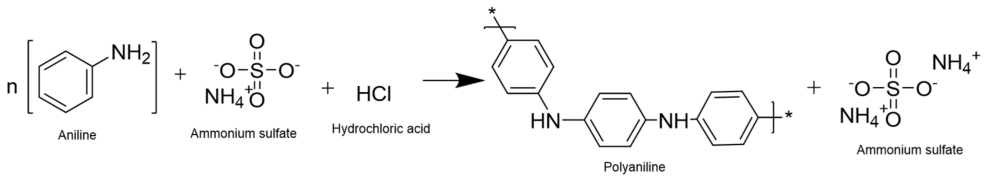

Scheme 1. Reaction showing polymerisation of aniline to polyaniline (PANI). (*)-repeating unit of the polymer structure.

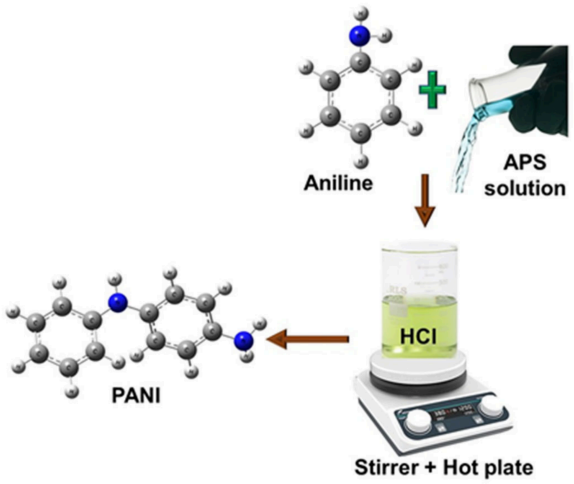

Figure 1. Synthesis of PANI nanomaterial.

2.3. Synthesis of PES

Polyethersulfone (PES) was synthesised through a nucleophilic aromatic substitution polycondensation reaction involving bisphenol A and bis(4-fluorophenyl) sulfone (BFS), reported by Nagane et al. [29]. Initially, precise amounts of bisphenol A and BFS were dissolved in 40 mL of the polar aprotic solvent dimethyl sulfoxide (DMSO). Potassium carbonate served as a dehydrating agent and base, promoting the deprotonation of bisphenol A and forming the active phenoxide nucleophile. The reaction mixture was agitated and heated under nitrogen to avoid oxidation and moisture contamination. The temperature was systematically increased to 80–100 °C and held steady for 1 h to facilitate reaction initiation. The temperature was then raised to 160 °C and held for 2 h to ensure complete polymerisation. Following the reaction, the viscous polymer solution was cooled and then poured into a large volume of methanol to facilitate precipitation of the PES. The product underwent filtration, followed by thorough washing with methanol and water to eliminate unreacted materials and salts, and was subsequently dried under vacuum at 60 °C. The synthesis reaction is illustrated in Scheme 2, and the procedure is summarised in Figure 2.

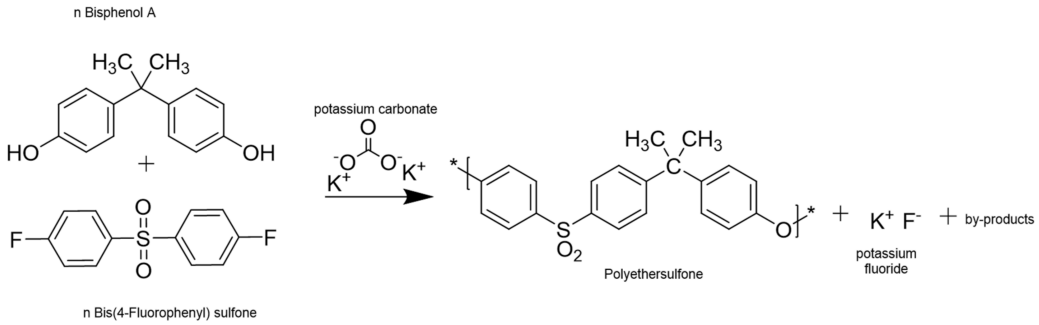

Scheme 2. Polymerisation reaction for PES formation. (*)-repeating unit of the polymer structure.

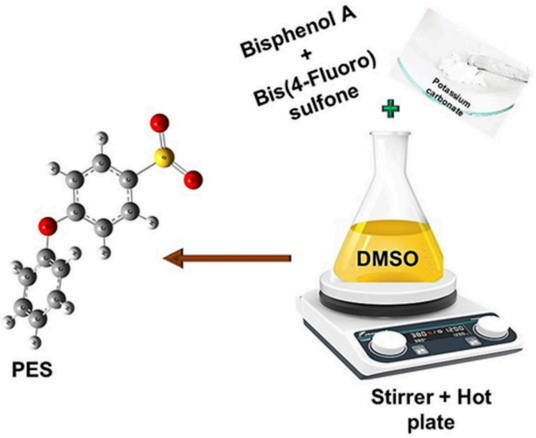

Figure 2. Pictorial illustration of PES synthesis.

2.4. Synthesis of PAMAM

The synthesis of PAMAM dendrimers was conducted using a divergent method, starting with ethylenediamine (EDA) as the core initiator. This method was adapted from the work of Lyu et al. [30]. The reaction unfolded through a series of iterative Michael addition and amidation steps. Initially, EDA was combined with an excess of methyl acrylate in methanol at room temperature for 48 h under constant stirring, yielding an ester-terminated half-generation (G0.5) intermediate. The product was subsequently purified using rotary evaporation to eliminate the solvent and any unreacted methyl acrylate. In the next phase, the G0.5 intermediate underwent amidation with an excess of EDA to produce a complete generation (G1.0) PAMAM dendrimer, once more under ambient conditions

for 48 h. The two-step process involving Michael addition followed by amidation was repeated to achieve higher generations (G3.0). A proposed reaction scheme is represented in Scheme 3, and a schematic illustration of the synthesis process is shown in Figure 3.

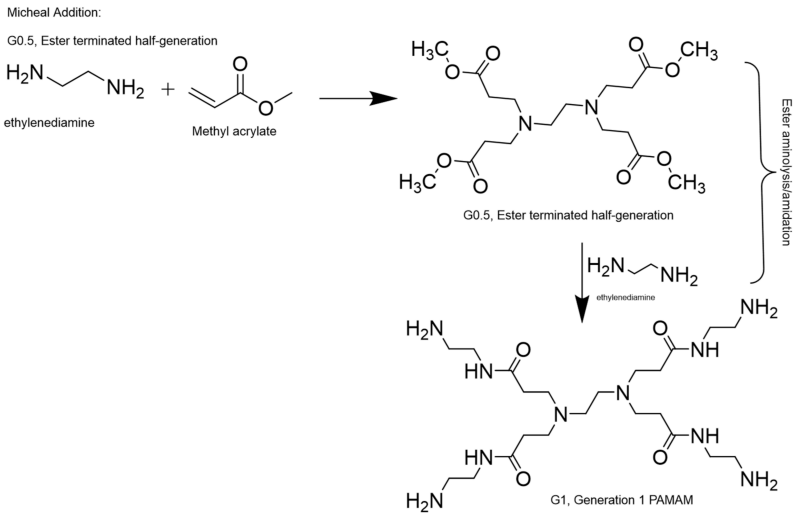

Scheme 3. Scheme illustrating Michael addition reaction for PAMAM formation.

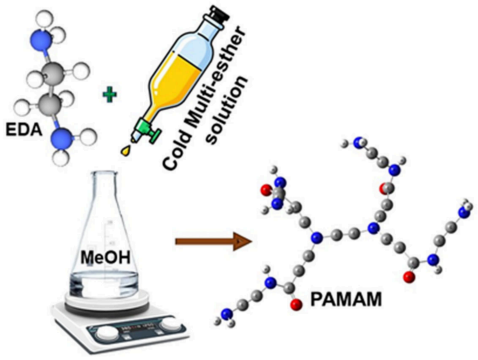

Figure 3. Illustration of PAMAM synthesis.

2.5. Density Functional Theory (DFT) Calculations

Density functional theory calculations were conducted for the three polymers (PANI, PES, and PAMAM) in conjunction with mercury ions. Additionally, optimised polymers incorporating mercury ions were introduced sequentially to the polymer surface, with a limit of three ions. These were designated as PES1Hg, PANI1Hg, PAMAM1Hg, PES3Hg, PANI3Hg, and PAMAM3Hg, respectively. The calculations utilised the B3LYP and 6-311G (d,p) as basis set for the polymers, while the LANL2DZ basis set was used for the Hg atoms and composites [31,32]. LANL2DZ basis set accounts for relativistic effects in the 5d shell of mercury. The software employed was Gaussian 09 [33]. GaussView 5.0.8 [23] was employed to visualise the optimised structures. All geometric parameters are fully optimised, and no imaginary frequencies are observed. The B3LYP method was selected due to its successful application in predicting and characterising the structural, electronic, and vibrational features of organometallics. Additionally, this method has proven to be one of the most accurate for both molecular and solid-state systems. Density-of-states (DOS) plots are generated using the GaussSum 3.0 software. It should be noted that the DFT calculations were performed on the dimeric and low-oligomeric models of PANI, PES, and PAMAM due to computational limitations with complete polymer chains. The B3LYP functional with the LANL2DZ potential and 6-311G(d,p) basis set was too expensive and could not accurately capture bulk attributes. The choice of oligomeric models is

supported by agreement with electrical characteristics relevant to coordination chemistry and the segregation of functional groups within amorphous polymers. Future work will include periodic density functional theory calculations with plane-wave basis sets, quantum mechanics/molecular mechanics embedding, and molecular dynamics simulations. This work provides a first-step assessment to identify reactive coordination sites and map electronic hierarchies in the polymers. Additional calculations are planned to confirm these findings with more advanced computational methods.

The DFT calculations yielded the electron densities of the highest occupied molecular orbital (HOMO) and the lowest unoccupied molecular orbital (LUMO), along with the optimised geometry, which illustrated the interactions between the different polymers and the mercury atoms. Furthermore, the energies of the highest occupied molecular orbital and the lowest unoccupied molecular orbital, as well as the optimised energy and dipole moment, were determined. The energies of HOMO and LUMO were utilised to calculate physicochemical descriptors, including but not limited to chemical hardness (η), softness (S), electrophilicity index (ω), and chemical potential (μ) (Equations (1)–(4)), where ε_L is the LUMO energy and ε_H is the HOMO energy.

$$\mu = \left(\frac{\partial E}{\partial N}\right)_{v(\underset{r}{\rightarrow})} \cong \frac{(\varepsilon_L + \varepsilon_H)}{2} \tag{1}$$

$$\eta = \frac{1}{2}\left(\frac{\partial^2 E}{\partial N^2}\right)_{v(\underset{r}{\rightarrow})} \cong \frac{(\varepsilon_L - \varepsilon_H)}{2} \tag{2}$$

$$S = \frac{1}{\eta} \tag{3}$$

$$\omega = \frac{\mu^2}{2\eta} \tag{4}$$

These calculations elucidate alterations in polymer characteristics upon mercury binding and the stability of that binding [34]. The estimation of the binding energies was conducted utilising Equation (5).

$$E_{B.E.} = E_{[\text{Polymer}-n\text{Hg}^{2+}]} - \left(E_{\text{Polymer}} + nE_{\text{Hg}^{2+}}\right) \tag{5}$$

In this context, $E_{B.E}$ indicates the binding energy, whereas $E_{complex\ (Polymer-n\text{Hg}^{2+})}$ refers to the total energy of the optimised composites, polymer–nHg. The terms $E_{Polymer}$ and $E_{n\text{Hg}^{2+}}$ denote the energies linked to the optimised polymer and nHg^{2+} ions.

Dimeric model systems were used here to represent larger polymeric frameworks of PANI, PES and PAMAM. The motivation for this was computational constraints; the modelling of full-length polymer chains with elongated repeat units and complex branching structures is prohibitively expensive at the level of quantum-chemical accuracy used here (DFT with hybrid functionals and relativistic basis sets for Hg). We acknowledge that these dimeric fragments are only an approximation to the real polymeric materials, since they represent local electronic properties and interactions of functional groups, but they do not fully represent long-range cooperative effects, chain entanglement or morphological heterogeneity. The methods for the modelling of polymeric systems are becoming more sophisticated, including periodic boundary condition DFT calculations for infinite chains [34], molecular dynamics simulations with reactive force fields to study solvation and dynamic adsorption processes [35], coarse-grained and multiscale techniques for extended networks and QM/MM hybrid methods that incorporate quantum level binding sites into classical polymer environments [36]. These advanced techniques have been successfully applied in similar settings and could enhance the present results by providing

a better understanding of collective behaviour and adsorption mechanisms. Thus, the available dimeric models offer useful qualitative information on the binding affinity of Hg^{2+}, and their limitations should be taken into account. Future studies can improve the understanding of the composite by utilising more advanced computational frameworks to better capture the polymer–metal interactions.

2.6. Characterisation

Morphological studies of the synthesised nanomaterials were performed by means of scanning electron microscopy (SEM, HITACHI, SU 8020), while an EDX spectrum was obtained with a similar instrument. To enhance image resolution and contrast, a 5-nm-thick layer of platinum-palladium alloy was sputtered onto the samples (Quorum, Q150R). Powder X-ray diffraction (XRD) patterns were recorded on a Rigaku D/max RB X-ray diffractometer using graphite monochromatized high-intensity Cu Kα radiation (λ = 0.15406 nm) in the 2θ range from 3° to 80°. Fourier transform infrared spectroscopy (FTIR) spectra of the samples were recorded using a PerkinElmer Spectrum 100 spectrometer fitted with a universal attenuated total reflectance (ATR) accessory over the wavenumber range of 4000–500 cm^{-1}. The UV-vis absorption spectrum of the prepared polymers was obtained from a DR 5000 UV–Vis spectrophotometer equipped with a cuvette compartment for placing the sample. ChemDraw Professional 15.0 software was used to draw the 2D structures of the synthesised polymers and the reaction schemes.

3. Results

3.1. SEM Analysis

Figure 4a–c presents SEM micrographs of PANI, PES, and PAMAM, respectively. Figure 4a illustrates a rough granular morphology characterised by enhanced cohesion and aggregation compared to the morphology observed in other materials. The observed nanostructured properties significantly enhance adsorption and ion transport, rendering PANI exceptionally effective for environmental remediation applications. Investigations into PANI nanostructured materials consistently reveal comparable morphologies, linked to enhanced conductivity and surface area, making them suitable for practical applications in adsorption and sensing [17,22]. This observed phenomenon in PANI has been widely reported in the literature and is attributed to π–π stacking between neighbouring oligomeric aniline chains during oxidative polymerisation. This is corroborated by the HOMO localisation analysis (seen in a later section), which shows that the HOMO of PANI is fully located on the sp^2 aromatic carbon skeleton and the delocalised π-electrons of the quinoid/benzenoid repeat units. The π-electron delocalisation allows chain aggregation, which explains the granular SEM appearance, in addition to the aryl-ring-based bidentate coordination of Hg^{2+} as expected for the PAN1Hg and PAN3Hg complexes (see Section 4.4). Thus, the major binding site for Hg^{2+} identified by DFT analysis is also the structural origin of the macroscopic porous morphology observed by SEM.

The micrograph in Figure 4b shows a PES micrograph exhibiting a clustered, particulate structure with large aggregates and some interstitial voids, which enhances its ability to trap and anchor particles. The uneven surface features enhance permeability and mechanical strength while also providing sites for the incorporation of functional groups, thereby improving adsorption characteristics. Based on our theoretical calculation, the HOMO analysis shows that the electron density is mainly localised at the two aryl rings attached to the C-O-C bridge, whereas the LUMO spreads towards the aryl-sulfonate ring (Section 4.2). The electronic topology shows that PES exposes its HOMO-rich aryl-ether regions at the polymer surface, consistent with the bidentate coordination at the electron-rich site observed in PES1Hg. Hence, the large aggregate surface areas observed in the

SEM image provide physical access to the electron-rich coordination sites identified by DFT analysis. In addition, the sulfone-rich surface was validated by EDX (S-peak) and SEM surface topology. The tridentate PES3Hg coordination mode can be correlated with the sulfone-rich surface, in which the lone pairs of sulfone oxygen atoms act as additional soft-intermediate donor sites for Hg^{2+}.

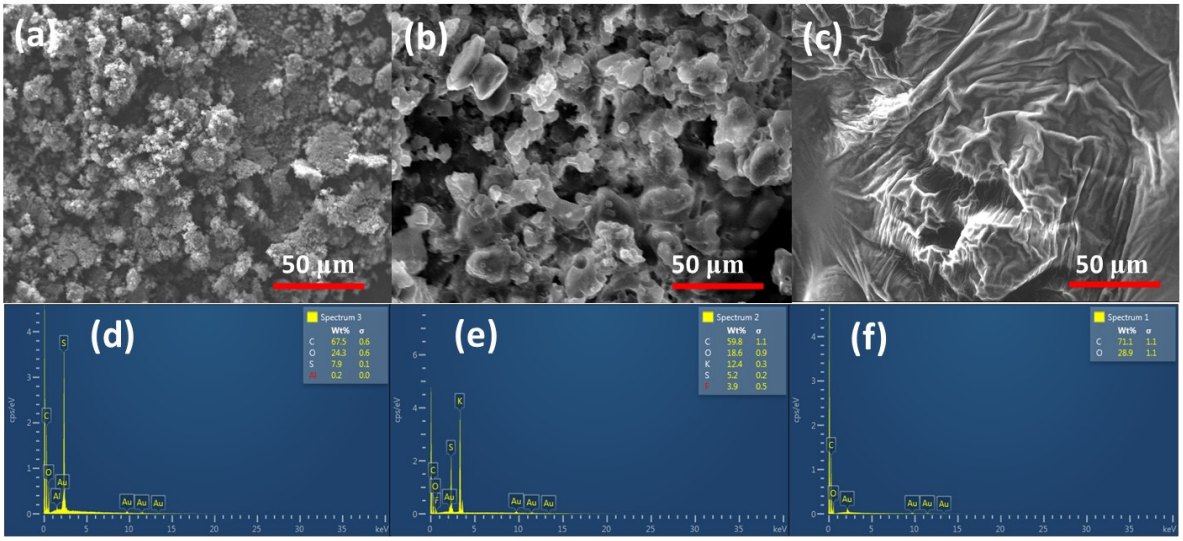

Figure 4. (**a**–**c**) Micrographs of PANI, PES and PAMAM, respectively; (**d**–**f**) EDX spectra of PANI, PES and PAMAM, respectively.

While Figure 4c illustrates the micrograph of PAMAM. The material exhibits a textured, stratified surface, which results from the aggregation of dendrimers and the self-assembly process that leads to fold formation during processing. The presence of wrinkles and surface grooves enhances host capacity and increases surface area for chemical adsorption and nanoparticle integration, making it ideal for scaffold applications and environmental remediation [17]. Alamos-Musre et al. [37] introduced a PAMAM dendrimer characterised by layered, wrinkled sheet morphologies, which correlate with enhanced mechanical strength and adsorption capacity. Furthermore, the wrinkled topology induces re-entrant pores and cavities that physically mimic the interior voids of the dendrimer, which DFT suggests as secondary coordination sites for Hg^{2+} (involving interior amide groups in addition to terminal $–NH_2$). The elemental makeup of nitrogen, oxygen, carbon and hydrogen obtained by the EDX spectrum is in exact agreement with the oligomeric PAMAM fragment predicted by DFT. The strong N Kα EDX signal indicates that the PAMAM surface has a significant concentration of primary amines (terminal $–NH_2$) and secondary amines/amides (interior C(=O)–NH). These are the main electron-rich (negative potential) locations for Hg^{2+} chelation shown on the ESP map. This gives a direct quantitative link between the EDX elemental mapping and the DFT electronic structure. The N-rich surfaces observed by EDX correspond directly to the N-lone-pair donor atoms identified computationally as the binding sites for Hg^{2+}. Conclusively, the EDX spectra shown in Figure 4d–f validate the presence of all anticipated elements in the synthesised nanomaterials.

3.2. XRD Analysis

Further details on the structures of PANI and other nanostructured materials were obtained through powder X-ray diffraction (XRD) measurements, which were used to analyse and provide insights into the morphology and crystallinity of the polymers [38]. The XRD results for PANI, alongside those of the other analysed materials, are presented in Figure 5. The notable crystalline peaks identified at 2θ = 20.12°, 24.24°, and 27.30°

correspond to the (020), (200), and (121) crystal planes of PANI in its emeraldine salt form. The observed peaks signify distinct areas within an amorphous matrix [39]. Figure 5 presents the diffractogram of PES powder, revealing that this polymer predominantly exhibits an amorphous structure. The data displays broad features alongside sharp peaks at 2θ = 18.4°, 28.40°, and 29.25°. It is noteworthy that PES can exhibit semicrystalline properties that may vary with processing conditions, composites, and additives. Observations of peaks at low angles indicate the presence of short-range order or crystalline microdomains within the amorphous matrix. Similar broad XRD features were reported by Motlokoa et al. [14]. The PAMAM analysis shows broad amorphous peaks at 2θ = 19.74°, 57.50°, and 68.84°. The observed peaks are characteristic of PAMAM dendrimers, which exhibit limited crystallinity due to their hyperbranched molecular structure. The lack of clear diffraction peaks indicates a material characterised by significant disorder. The findings of Al-Gamal et al. [18] indicate that PAMAM generally exhibits a broad band in the XRD pattern at approximately 2θ of 21°, which signifies an amorphous polymeric phase. This is associated with significant molecular flexibility and is well-suited for applications involving adsorption and surface reactivity, aligning with its use in environmental remediation or as a host in nanocomposites. In conclusion, these interpretations underscore the appropriateness of the prepared polymers for environmental applications.

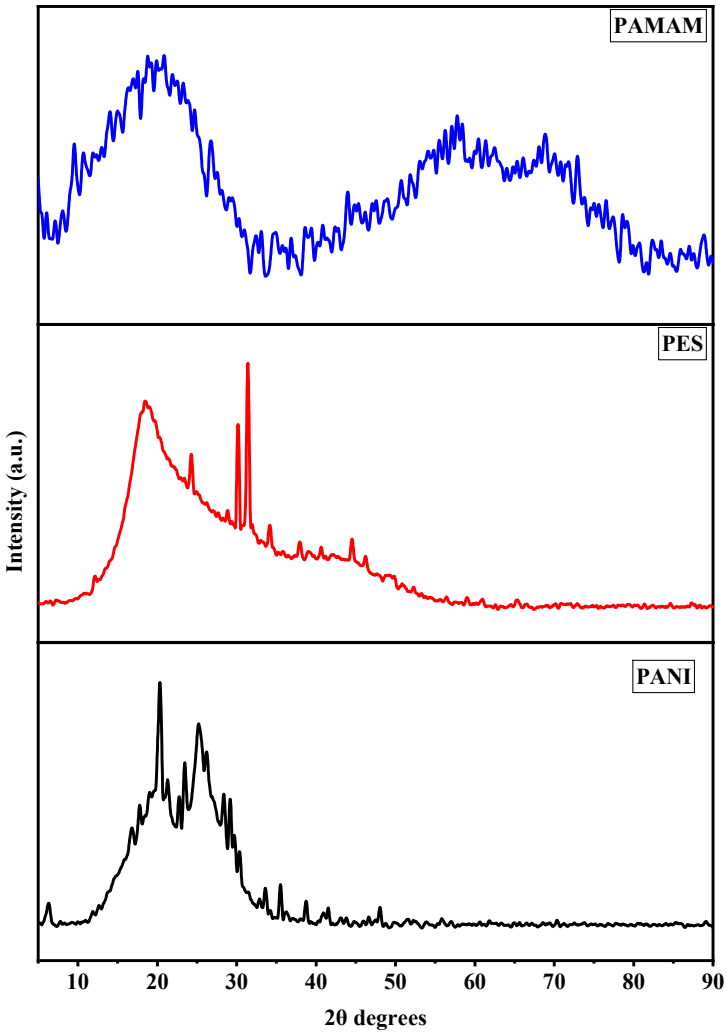

Figure 5. XRD diffractogram of PANI, PES and PAMAM.

3.3. UV–Vis Analysis

The absorption spectra of PANI, PES, and PAMAM are presented in Figure 6a–c. In Figure 6a, the UV spectra of the PANI reveal an absorbance peak at 270.18 nm, accompanied by a shoulder peak at 314.12 nm. These features are associated with π–π* transitions in aromatic rings [17,18]. In addition to these peaks, there exists a minor free electro-absorption tail near 391.23 nm, which can be identified as the conductive form of PANI [17]. The absorption band near 600 nm is associated with the intramolecular electronic transition occurring between the quinoid and benzenoid units [16]. This band at 270.18 nm is commonly documented for PANI and PANI-based composites. The peak observed at 314.12 nm is occasionally characterised as π→π* or polaron-π*, contingent upon the oxidation or doping level. The precise location is heavily influenced by factors such as oxidation state, protonation (doping), and the polymer chain's conformation. This suggests that the PANI was in the emeraldine state, consistent with the XRD findings. Numerous recent investigations of PANI have revealed a consistent long-wavelength characteristic. The multi-band absorption features are in perfect agreement with the DFT frontier orbital model: the HOMO of PANI is localised on the π-conjugated sp^2 carbon backbone and the bridging N atoms, but the LUMO is delocalised over the same aromatic system. The modest HOMO–LUMO gap computed for PANI, the second narrowest among the three polymers (Egap: PES > PANI > PAMAM), is in agreement with the lowest energy absorption measured at around 600 nm. The UV–Vis spectrum supports the protonation state used for the DFT model and this suggests the presence of the emeraldine salt state.

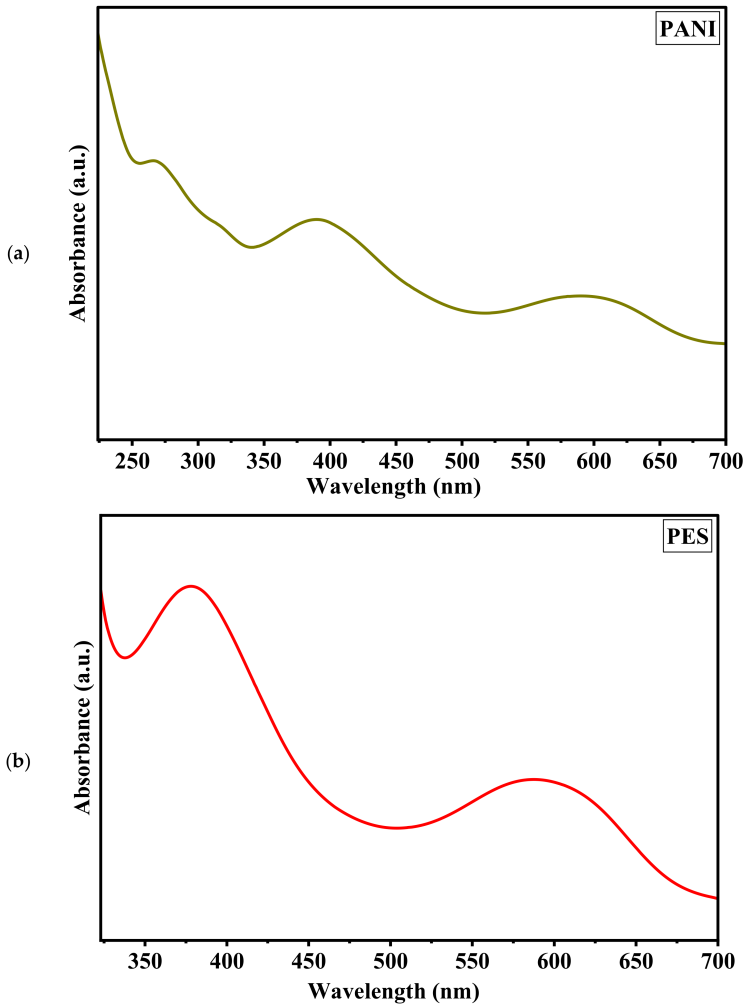

Figure 6. *Cont.*

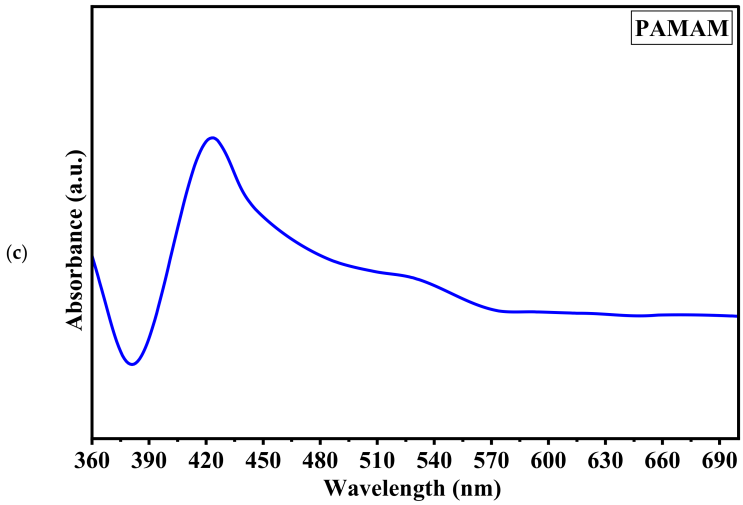

Figure 6. UV–Vis spectra of (**a**) PANI, (**b**) PES and (**c**) PAMAM.

The PES UV–Vis spectra (Figure 6b) exhibit absorption at 377.95 nm, which corresponds to π→π* transitions of the aromatic sulfone/sulfone-linked phenyl rings, thereby confirming the characteristic optical fingerprint of PES. This band is frequently utilised in membrane studies as a monitoring wavelength and is present in numerous PES characterisation reports [20]. Additionally, the absorption observed at 599.15 nm falls within the visible spectrum, consistent with the existing literature [38]. Furthermore, it is generally noted exclusively in diphenylsulfone. The energy separation between these orbitals, observed experimentally as the UV–Vis absorption edge at 377.95 nm, indicates the largest HOMO–LUMO gap among the three polymers. In the context of adsorption reactivity, this larger gap indicates a reduction in reactivity and an increase in the kinetic stability of the PES adsorbent structure, aligning with PES being the most chemically resilient of the three polymers. Nonetheless, the PES ESP map verifies that the lone pairs of the sulfone oxygen and the aryl-ether bridge continue to possess adequate electron density for the coordination of electrophilic Hg^{2+}, even with the increased gap.

In the case of PAMAM, two distinct peaks are observed at 422.34 nm and 530.33 nm (Figure 6c). The peak observed at 422.34 nm corresponds to molecules containing organic amides or amines, as well as dendrimers, and indicates π→π* transitions of amide or aryl fragments or n→π* transitions of amide chromophores. Investigations into PAMAM dendrimers typically indicate absorbance within the 300–420 nm range. The narrowest HOMO–LUMO gap corresponds to the lowest absorption energy (longest wavelength) among the three polymers, confirming experimentally that PAMAM is the most electronically polarisable and reactive of the three systems. This is consistent with the DFT prediction that PAM1Hg has the largest binding energy (−85.68 eV) for the single-Hg^{2+} complexes. The experimental UV–Vis data are quantitatively consistent with the DFT orbital gap energetics. The polymer with the lowest-energy UV–Vis absorption (PAMAM) also has the narrowest DFT-computed Egap and the greatest Hg^{2+} binding affinity at low loading.

3.4. FTIR Analysis

The functionalities of the prepared polymer nanomaterials are analysed and illustrated in Figure 7. The absorption bands of PANI feature peaks at 613 cm^{-1} and 1121 cm^{-1}, which correspond to the out-of-plane C-H and in-plane C-H bending modes, respectively. The peak observed at approximately 1289 cm^{-1} corresponds to the conducting protonated form, as it is attributed to the C-N•$^{+}$ stretching mode in the polaron form of PANI. The bands observed at 1490 cm^{-1} and 1570 cm^{-1} correspond to the stretching modes of C=C and C=N in the benzenoid and quinoid groups of the PANI, respectively. The peak ob-

served at 1315 cm^{-1} corresponds to a C–N stretching mode associated with the benzenoid unit. The absorbance band observed at 2843 cm^{-1} is indicative of an aromatic C-H stretch, whereas the peak at 2923 cm^{-1} is associated with the N-H stretching mode of an aromatic amine. The N-H and C=N groups facilitate robust coordination with metal ions by donating lone electron pairs. The quinoid (C=N) and benzenoid structures enable redox interactions, which support both adsorption and partial reduction in Hg^{2+}. The C=O and C–N groups observed at approximately 1680 cm^{-1} and 1300 cm^{-1} could serve as secondary binding sites, potentially improving selectivity by forming stable complexes with mercury. Singh et al. [39] showed that PANI-based composites utilise these functional groups for the swift binding of Hg^{2+}.

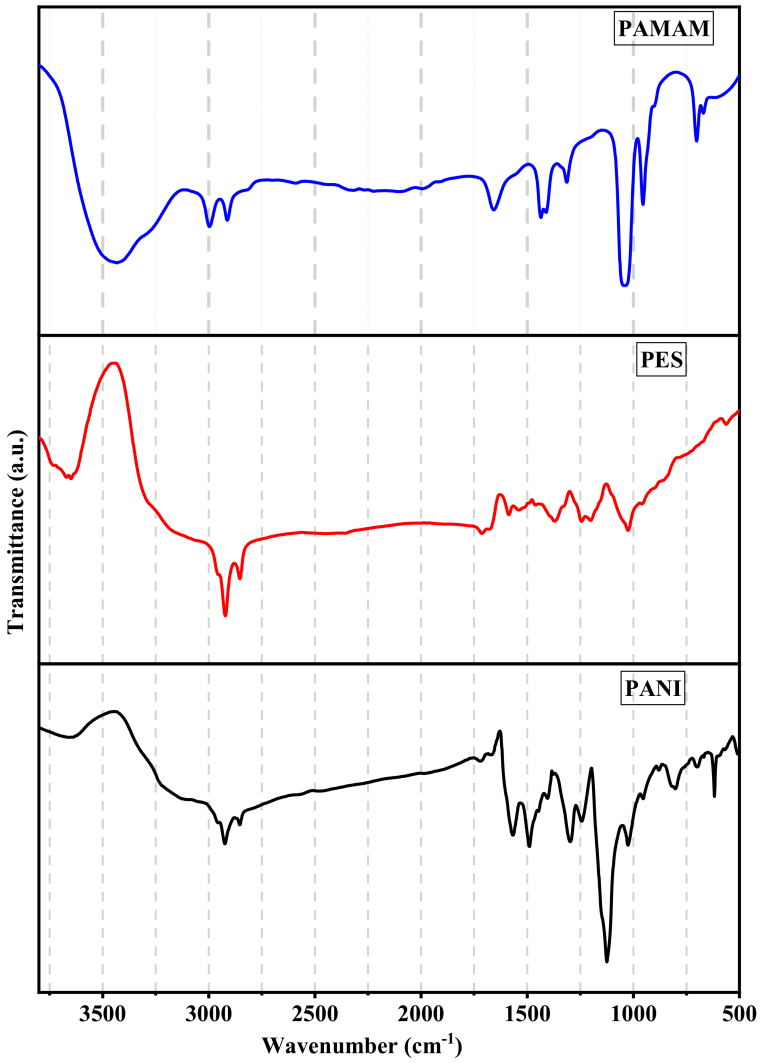

Figure 7. FTIR spectra of PANI, PES and PAMAM.

Figure 7 illustrates the peaks associated with the PES polymer. The peak at 552 cm^{-1} corresponds to the C=C stretching vibration within the aromatic ring. The peaks observed at 1188 cm^{-1}, 1362 cm^{-1}, and 1583 cm^{-1} can be assigned to the sulfonyl (O=S=O) group, whereas the peak at 1228 cm^{-1} corresponds to the aromatic ether (C-O-C) group. FTIR has been widely employed to analyse the chemical composition related to the surface modification of PES-modified membranes [40,41]. The S=O moiety imparts polarity and hydrophilicity to the PES surface, enhancing wetting and accessibility. Sulfone groups participate in weak coordination, but, more importantly, they facilitate the immobilisation of metal-binding functional groups on the membrane surface. The spectra of PAMAMA

in Figure 7 exhibit O-H at 3446 cm^{-1}, N-H stretch at 2990 cm^{-1}, C-H at 2910 cm^{-1}, C-N at 1290 cm^{-1}, N-H at 1670 cm^{-1}, and C=C at 954 cm^{-1}. The presence of Amide I (C=O) at approximately 1650 cm^{-1} and Amide II (N-H bend) at around 1423 cm^{-1} validates the amide-rich dendrimer backbone, which is essential for chelation and branching. The broad stretches of N-H and O-H are indicative of significant hydrogen bonding present in dendrimers. In the spectra of PAMAM nanocomposites, N-H bands were identified at 3362 cm^{-1} and the amide I band at 1648 cm^{-1}, as reported in [42]. Additionally, Ban et al. [43] observed similar peaks for N-H at 3371 cm^{-1}, C=O at 1650 cm^{-1}, and C-N at 1288 cm^{-1} in their report. The presence of primary/secondary amines and amide groups facilitates a high density of terminal amines and interior amide groups that can chelate metal ions like mercury. This configuration provides multiple binding sites for multivalent cage-like complexation, effectively trapping Hg^{2+}. The C-N group enhances additional binding by stabilising complexed cations via electron-rich nitrogen donors. Consequently, the findings indicate that the synthesised polymers exhibit distinct peaks characteristic of their composition.

4. Theoretical Studies of the Prepared Polymers

This section examines the DFT studies of the polymers, with results compared to experimental findings. The interaction of optimised polymer molecules with mercury is examined to predict their potential adsorption mechanism and their application in environmental remediation. The investigation utilises the LANL2DZ and B3LYP methodologies, along with a 6-311G(d,p) basis set. This study provides a detailed analysis of vibrational frequencies, electrostatic potentials (ESPs), and contour plots. The frontier molecular orbital theory indicates that the interactions between the HOMO and LUMO of the interacting species play a crucial role in determining chemical reactivity [31]. For example, according to the Koopman theorem [32,44], one can estimate the negative value of the HOMO energy level as the ionisation potential (IP). Additionally, a range of quantum-chemical parameters was computed to deepen our understanding of the intermolecular interactions in the optimised molecules, particularly those associated with the complex formed between the polymers and mercury atoms. Figure 8 illustrates the optimised structures of the molecules employed in this study.

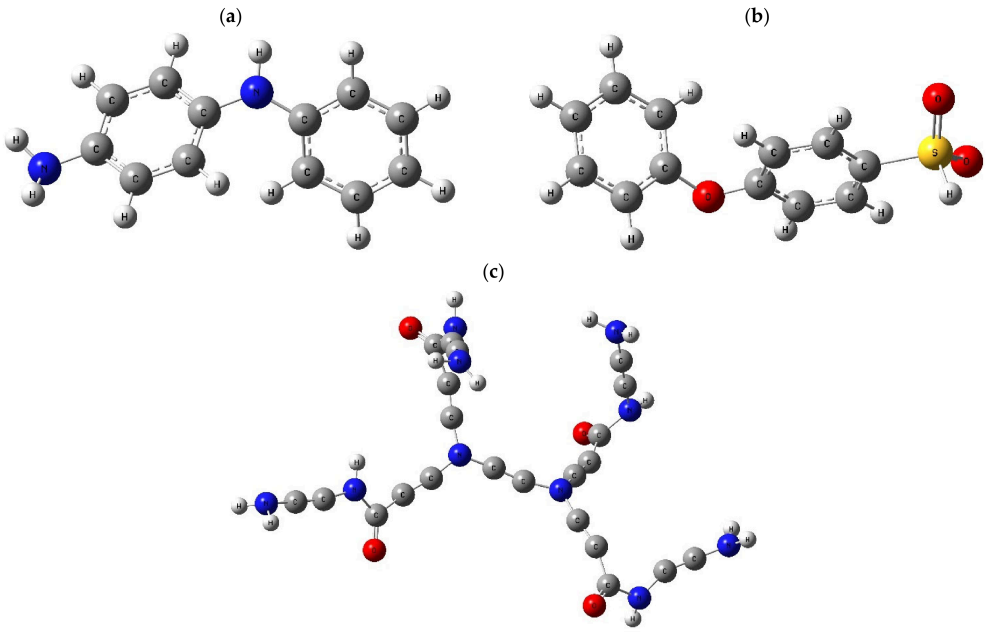

Figure 8. Optimised structure of (**a**) PANI, (**b**) PES and (**c**) PAMAM.

4.1. Molecular Vibrational Frequency

Figure 9 illustrates the simulated theoretical vibrational frequencies, emphasising the functional groups present in the simulated materials: PANI, PES, and PAMAM. The notable infrared (IR) frequencies observed in PANI feature a peak at 3156 cm^{-1}, signifying an N-H stretching vibration linked to the existence of an amino group. The observed peaks at 1644 and 1564 cm^{-1} are indicative of the stretching deformation associated with the quinone and benzene rings, respectively. The absorption bands observed at 1344 and 1304 cm^{-1} are attributed to C-N and quinoidal C=N bonds, respectively. The peaks noted at 1151 and 838 cm^{-1} reflect the in-plane and out-of-plane bending vibrations linked to the polyaniline benzene ring, respectively.

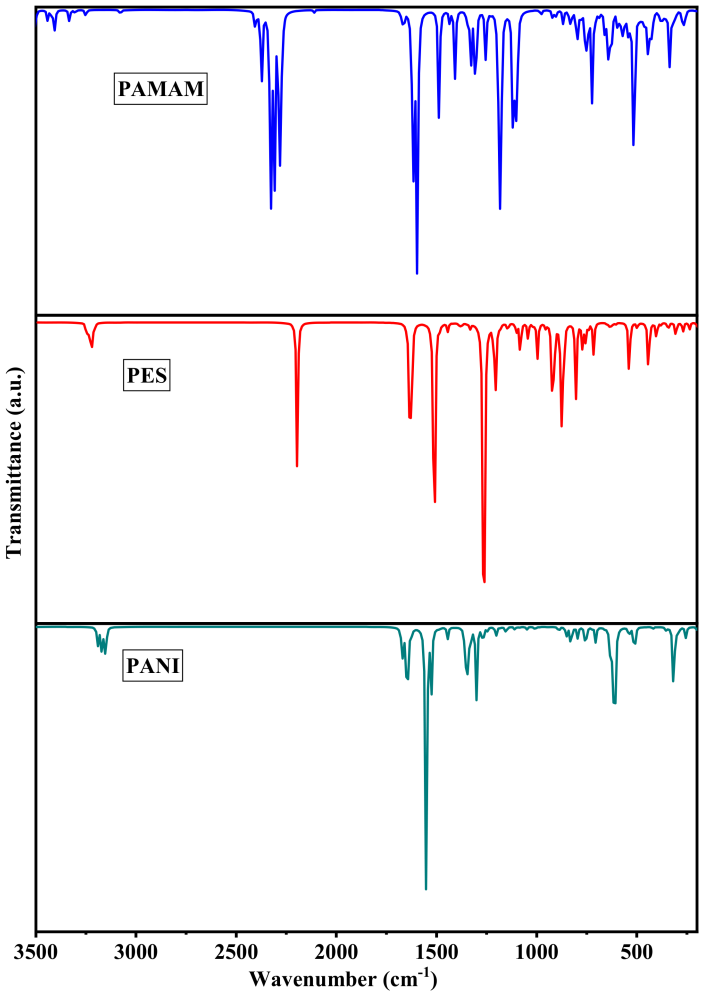

Figure 9. Theoretical vibrational spectra of simulated molecules, PANI, PES and PAMAM.

The vibrational frequencies computed by DFT for the PANI tetramer reproduce these features with high fidelity: N-H stretch at 3156 cm^{-1} (experiment: 2923 cm^{-1}; Δ = 233 cm^{-1}, 7.4%), C=N quinoid at 1304 cm^{-1} (experiment: 1289 cm^{-1}; Δ = 15 cm^{-1}, 1.2%), C=C benzenoid at 1564 cm^{-1} (experiment: 1490 cm^{-1}; Δ = 74 cm^{-1}, 5.0%), C–N at 1344 cm^{-1} (experiment: 1315 cm^{-1}; Δ = 29 cm^{-1}, 2.2%) and in-plane C-H at 1151 cm^{-1} (experiment: 1121 cm^{-1}; Δ = 30 cm^{-1}, 2.7%). This persistent overestimation of the N-H stretch frequency (7.4%) is a known artefact of DFT calculations in the gas phase, where the absence of intermolecular hydrogen bonding and solvent effects results in an artificial stiffening of the N-H stretching force constants. Using a standard scaling factor of 0.961 (recommended for B3LYP/6-311G(d,p)) reduces this difference to ~1.3%. FTIR-identified functional groups provide predictions in coordination chemistry, especially for N-H and C=N groups, which are the main HOMO-

density sites that interact with metal ions, contributing lone electron pairs. The characteristic red-shifts in the quinoid C=N band (~200 cm^{-1}) and C-N stretching vibrations are observed in PANI after Hg^{2+} adsorption, which are attributed to the redistribution of electron density. The extent of these red-shifts agrees with N→Hg^{2+} coordination strengths, as shown by the calculated bidentate binding energies of PAN1Hg (0.063 eV, 6.04 kJ mol^{-1}) and PAN3Hg (0.065 eV, 6.30 kJ/mol) The FTIR evidence for N-centred coordination is consistent with DFT predictions that mercury forms bidentate complexes that alter electron density and result in frequency shifts upon adsorption.

Consequently, the computational results exhibited spectral patterns that are in close agreement with those documented in the literature [45]. The vibrational frequencies of PES depicted in Figure 9 exhibit notable peaks attributed to the aromatic bands at 1638 and 1504 cm^{-1}, which are characteristic of the benzene ring and C-C bond stretching, respectively, in addition to the aromatic ether band located around 1264 cm^{-1}.

The DFT calculations of the PES dimer reproduce the aromatic stretches at 1638 cm^{-1} (benzene ring, experimental value: 1583 cm^{-1}; difference = 55 cm^{-1}, 3.5%) and 1504 cm^{-1} (C-C bond, experimental value: 1490 cm^{-1}; difference = 14 cm^{-1}, 0.9%) and the aromatic ether band at 1264 cm^{-1} (experimental value: 1228 cm^{-1}; difference = 36 cm^{-1}, 2.9%). The ESP map shows that the main negative-potential (electron-rich) area of the PES molecule is located on the sulfone oxygen atoms and the aryl-ether bridge—these are exactly the functional groups detected experimentally by FTIR at 1188–1362 cm^{-1} and 1228 cm^{-1}. The S=O moiety withdraws electron density from the aromatic ring, but still has a significant lone-pair density on the oxygen atoms. This feature places the sulfone O atoms as the PES counterpart to the N atoms in PANI, and they operate as the major coordination donors for Hg^{2+}. Therefore, the bidentate PES1Hg coordination mode (DFT: binding at the electron-rich location of the molecule, involving the aryl-ether and sulfone moieties) is in tandem with the functional groups detected by FTIR. In analogous experiments, post-adsorption FTIR of PES-based materials consistently shows broadening and red-shifting of the S=O asymmetric stretching band as diagnostic evidence for S=O$\cdots$$Hg^{2+}$ coordination.

The vibrational frequencies of PAMAM include O-H at 3409 cm^{-1}, N-H at 3256 cm^{-1}, and C-H at 3063 cm^{-1}. The detection of Amide I (C=O) near 1604 cm^{-1} and Amide II (N-H bend) close to 1443 cm^{-1} confirms the presence of an amide-rich dendrimer backbone, which is crucial for chelation and branching. The peaks that are left are attributed to C-N at 1237 cm^{-1} and C=C at 1098 cm^{-1}. Table 1 compares peak frequencies obtained from experimental and theoretical simulations. The prominent peaks observed in the experimental findings for individual polymers closely match those in our theoretical studies.

The agreement between experimental and computational results for the amide bands (Amide I and II, with deviation less than 3%) is very relevant, as the amide C=O and N-H groups are the main binding sites for Hg^{2+} in PAMAM-based adsorbents. The ESP map of PAMAM shows a large negative potential region around the C=O moiety, indicating that it is the principal site of electrophilic attack by Hg^{2+}. The positive charge, however, is confined to the –NH_2 terminal groups. Studies on PAMAM-Hg^{2+} adsorption consistently indicate that the primary binding sites for Hg^{2+} are the functional groups –NH_2, C(=O)NH, C–N, O–H, C=O and C–N. This is confirmed by post-adsorption FTIR measurement, revealing typical changes at the Amide I and N-H locations. The functional groups identified as binding locations in these experimental tests match exactly, functional group by functional group, the sites indicated by the DFT ESP map and the HOMO localisation of the PAMAM model. Thus, the computational findings exhibited spectral patterns that closely matched the experimental outcomes and those documented in the literature [45].

Table 1. Comparison of experimental and theoretical vibrational frequency assignment.

	Frequencies of Prepared Polymers (cm^{-1})					
	PANI		PES		PAMAM	
	Exp	Cal	Exp	Cal	Exp	Cal
N-H stretching	2923	3156	-	-	2990	3256
out-of-plane C-H bending	613	838	-	-	-	-
in-plane C-H bending	1121	1151	-	-	-	-
C-N and quinoidal C=N bonds	1315, 1570	1344, 1304	-	-	1290	1237
C-C bond stretching	-	-	1511	1504	-	-
stretching modes of C=C	1490	1445	552		954	1098
aromatic C-H stretch	2843	2898	-	-	2910	3063
C=O	1680				-	-
sulfonyl (O=S=O) groups	-	-	1188, 1362, and 1583	1256	-	-
aromatic ether (C-O-C)	-	-	1228	1189	1264	
O-H	-	-	-	-	3446	3409
Amide I (C=O) and Amide II (N-H bend)	-	-	-	-	1650 and 1423	1604 and 1443

4.2. Orbital and Quantum-Mechanical Analysis

Figure 10 illustrates the unique localisation of the molecular orbitals (MOs), specifically the HOMO and LUMO, in PANI, PES, and PAMAM. The HOMO and LUMO of PANI are located around the sp^2 carbon that forms the aromatic rings, as well as around the delocalised π-electron present within the aromatic rings of the molecules, respectively. The highest occupied molecular orbital of the PES molecule is predominantly concentrated around the two aromatic rings that intersect the C-O-C bridge, whereas the lowest unoccupied molecular orbital is situated more towards the aryl-sulfonate ring. The HOMO of PAMAM is localised primarily around one arm of the dendrimer and partially around the carbon–carbon bond of the amine backbone. Notably, the LUMO is situated around two arms of the dendrimer, extending through the amine backbone to another arm of the dendrimer. The electronic localisations observed in the polymers under investigation indicate that the molecules can engage in electrochemical interactions with other molecules.

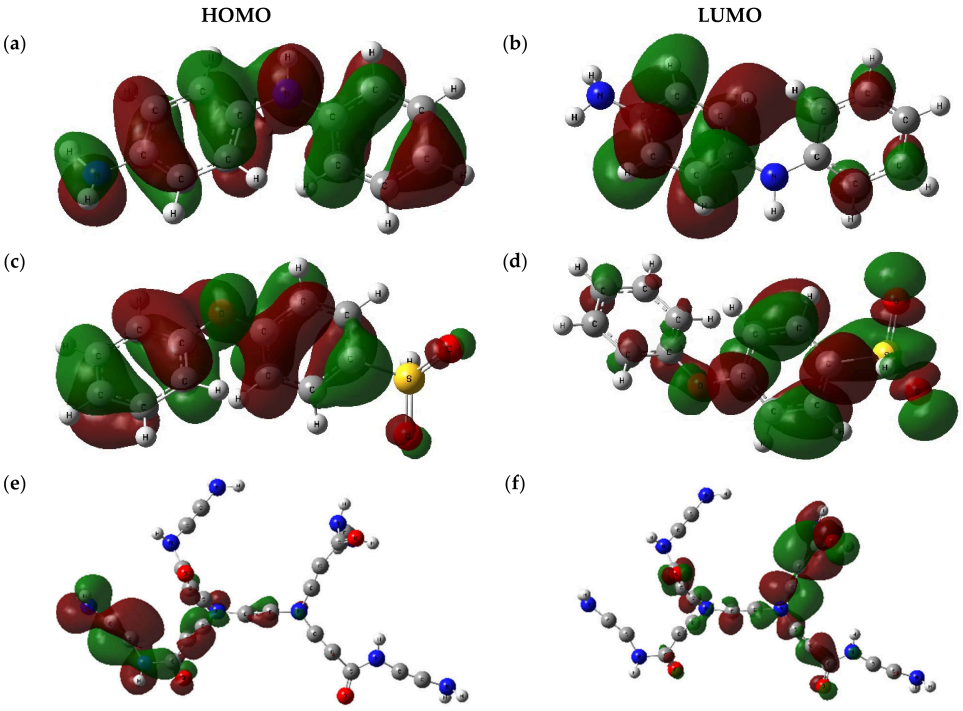

Figure 10. Frontier molecular orbital; HOMO–LUMO: (**a**,**b**) PANI, (**c**,**d**) PES, and (**e**,**f**) PAMAM, respectively.

The relative energies of the molecular orbitals are essential for comprehending a molecule's chemical behaviour. The HOMO–LUMO gap plays a crucial role in fundamental properties, including stability, reactivity, electronic properties, and electrochemical reactions. Wider gaps lead to decreased polarisability, which in turn diminishes chemical reactivity and enhances stability. Furthermore, these properties assist in forecasting the reactions of the polymers with other molecules they may encounter [46]. The pertinent parameters for PANI, PES, and PAMAM have been calculated and are displayed in Table 2. The calculated HOMO and LUMO energies for the three polymers exhibit significant variations (Table 2). The E_g values are organised in descending order as follows: PES > PANI > PAMAM. Consequently, the PAMAM polymer exhibits a superior electron-donating capability (indicated by a lower ionisation energy) and a greater propensity to acquire an electron (reflected in a higher electron affinity) compared to the other polymers. Notably, among the polymers analysed, PAMAM exhibits the smallest frontier orbital energy gap, indicating reduced chemical stability and, conversely, increased chemical reactivity, as well as the highest polarisability. A narrower E_{gap} indicates a system that is more electronically rigid, and such rigid systems tend to be smaller and exhibit lower polarisability compared to their softer counterparts [47]. Additionally, a larger E_g implies a higher-energy UV–Vis absorption onset, i.e., a less polarisable and more rigid material. In contrast, a smaller Egap causes a red shift in absorbance and a higher chemical reactivity towards metal ions. This is readily shown in the UV–Vis spectra, where PES shows absorption at 377.95 nm (lowest wavelength, broadest gap, hardest), PANI at ~600 nm (middle), and PAMAM at 530.33 nm (low-energy transition, in agreement with the narrowest gap). The UV–Vis absorption energies provide an experimental proxy for the DFT-derived HOMO–LUMO gaps, and the agreement in ordering suggests the electronic structure derived from DFT.

Table 2. Calculated quantum-chemical reactivity parameters.

Parameters (eV)	PANI	PES	PAMAM
E_{HOMO} (ε_H)	−0.1807	−0.2555	−0.2231
E_{LUMO} (ε_L)	−0.0111	−0.0614	−0.0953
Energy gap (ε_{gap})	0.1696	0.1941	0.1278
Ionisation energy (I.E)	0.1807	0.2555	0.2231
Electron affinity (E.A)	0.0111	0.0614	0.0953
Hardness (η)	0.0848	0.0971	0.0639
Softness (eV^{-1})	11.7950	10.2987	15.6495
Electronegativity (χ)	0.0960	0.1585	0.1592
Chemical potential (μ)	−0.0960	−0.1585	−0.1592
Electrophilicity (ω)	0.0540	0.1294	0.1983
Nucleophilicity (ε), eV^{-1}	18.5190	7.7279	5.0429
Back donation (ΔE_{bd})	−0.0210	−0.0243	−0.0159
Electron transfer (ΔN_{max})	1.1320	1.6323	2.4914
Fermi level (E_F)	−0.0960	−0.1585	−0.1592
Work function (Φ)	0.0960	0.1585	0.1592

The global reactivity characteristics, such as chemical potential, chemical hardness, global softness, electrophilicity index and maximal charge transfer, are directly obtained from the HOMO and LUMO energies estimated by DFT. While these are gas-phase values and cannot replace actual adsorption data, they do have a unique, experimentally testable physical meaning when combined with spectroscopic evidence and coordination chemistry.

Based on the Pearson Hard and Soft Acids and Bases (HSAB) theory, the chemical hardness (η) is an important parameter in the adsorption selectivity. For example, Hg^{2+} is shown to be a soft Lewis acid with a hardness of ~7.7 eV and, hence, tends to combine with

soft Lewis base donors with low hardness and high softness (*S*). Of the three polymers, PAMAM exhibits the maximum softness (lowest η), making it the most thermodynamically suitable donor for soft Hg^{2+} according to the highest single-mercury binding energy (PAM1Hg: −85.68 eV). This HSAB-based prediction agrees with experimental research showing that amine-rich PAMAM dendrimers can remove >90% of Hg^{2+} in competitive multi-ion environments. The electrophilicity index ω is a measure of the polymer's electron-accepting ability; a higher ω value indicates greater resistance to electron donation and, consequently, a weaker adsorbent character for cationic metal ions. This is consistent with PAMAM being a better electron donor to Hg^{2+} than PES, which has stronger electron-withdrawing sulfone groups and is more electrophilic. The determined ΔN_{max} value of 2.49 for the PAMAM indicates a significantly charged condition. This value exceeds the 1.96 reported by Duraikannu [48]. The analysis indicates that increased molecular softness and reduced energy gap correlate with elevated dielectric constants and electrical conductivity.

4.3. Electrostatic Potential (ESP) and Contour Mapping of Optimised Molecules

The arrangement of charge across the atoms in a complex affects the electrostatic potential, which plays a vital role in intermolecular interactions [49]. The ESP predicts the reactivity of a molecule or complex, indicating that regions of negative potential serve as sites for protonation and electrophilic attack, whereas areas of positive potential denote nucleophilic sites [50]. Figure 11a,c,e illustrates the ESP mappings for PANI, PES, and PAMAM materials, respectively. The colour scale (Figure 11) depicts positive values (far right, blue) and negative values (far left, red). The red colour code (negative value) signifies the lowest electrostatic potential, which is associated with loosely bound or excess electrons, making them susceptible to electrophilic attack. The blue colour indicates the peak electrostatic potential, highlighting an electron-deficient site that renders it vulnerable to nucleophilic attack.

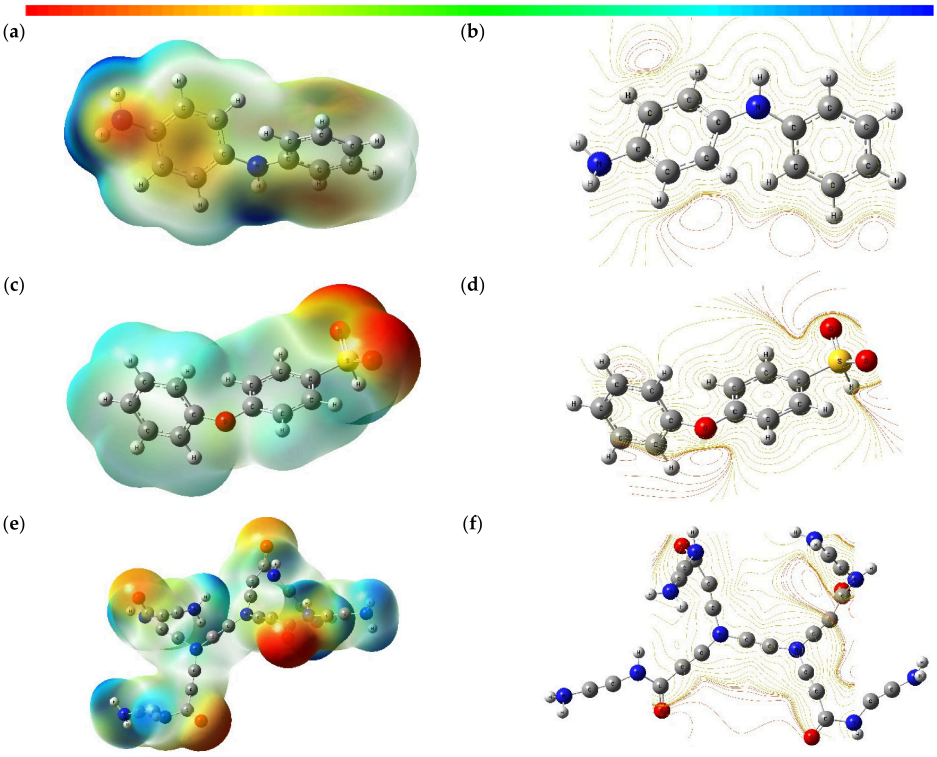

Figure 11. (**a**) ESP mappings of PANI, (**b**) contour mapping of PANI, (**c**) ESP mappings of PES, (**d**) contour mapping of PES, (**e**) ESP mapping of PAMAM and (**f**) ESP and contour mapping of PAMAM.

The PANI molecule exhibits a strong electronic distribution throughout its structure. The nucleophilic site is clearly localised mainly on the terminal NH_2 and near the bridge area. The electrophilic region is evenly distributed across the molecules. This indicates a robust ability for charge transfer within the molecule and a propensity to release an electron, facilitating potential electronic interactions with mercury or any nearby molecules. The ESP map of PANI illustrates negative potential localised at the terminal –NH_2 groups and N atoms bridging the benzenoid and quinoid rings, corresponding to active sites identified by FTIR (C=N at 1289 cm^{-1}, N-H at 2923 cm^{-1}). Upon Hg^{2+} adsorption, these sites show red shifts, indicating electron density redistribution away from N-H and C=N bonds, thus confirming the binding of Hg^{2+} at these N-donor atoms. The positive potential observed on the aromatic ring indicates π-acidic regions, which facilitate the reduction in Hg^{2+} to Hg^{+}/Hg^{0} on PANI surfaces due to the quinoid/benzenoid equilibrium.

The MEP map of PES reveals a significant build-up of positive charge on both aryl rings, suggesting a strong tendency towards nucleophilic attack, whereas the electrophilic site is focused on the sulfone moiety of the polymer. It appears that there is a significant probability of electrophilic attack at these locations, facilitating metal-ion binding, which is crucial for efficient mercury remediation. In PES, the ESP map shows strong positive charge on aryl rings and concentrated negative charge at the sulfone S=O moiety, aligning with FTIR showing O=S=O asymmetric stretching (1188–1362 cm^{-1}). Hg^{2+} binds to the electron-rich aryl-ether site via bidentate coordination (PES1Hg), targeting the highest electron-density region, while the tridentate PES3Hg complex includes sulfone oxygen, indicated by FTIR at 1188 cm^{-1} as a secondary coordination site.

It is noteworthy that the distribution of negative charge, indicative of nucleophilic sites, is concentrated in multiple regions, primarily around the C=O moiety on the PAMAM polymer. The NH_2 group is primarily responsible for the positive charge, serving as the electrophilic site. The comprehensive electronic distribution surrounding the molecule indicates a significantly enhanced affinity for binding with metal ions. This indicates a more effective elimination of mercury from wastewater. The MEP maps highlight the polymers' strong potential for mercury remediation, characterised by their significant attraction and binding affinity for metal ions. The PAMAM ESP map reveals an extensive negative potential around the C=O moiety of amide groups and through the amine backbone, reflecting the dendrimer's multi-site nature. It predicts that Hg^{2+} will be encaged by cooperative N-H and C=O donors, supporting a multidentate chelation mechanism, as confirmed by studies showing over 90% Hg^{2+} removal via a cage-like complex. Coordination transitions from monodentate PAM1Hg at low concentrations to tridentate PAM3Hg at higher loadings, reflected in FTIR band shifting as Hg^{2+} concentrations increase on PAMAM adsorbents.

The charge distribution observed in the analysed polymers is supported by the contour maps related to each polymer, as illustrated in Figure 11b,d,f. This anticipated interaction is projected to facilitate efficient mercury removal, thus improving environmental remediation efforts.

4.4. Polymer–Mercury Interaction Studies

4.4.1. Optimised Molecules and Molecular Interaction

The interaction of optimised polymer molecules with mercury molecules can predict their potential adsorption characteristics and mechanisms for wastewater remediation applications. The analysis utilises the LANL2DZ and B3LYP methodologies, along with a 6-311G(d,p) basis set. The binding energy and the interaction plots of frontier molecular orbitals are elaborated upon in this section and the subsequent subsection, respectively. Figure 12 presents the optimised complexes that are formed between the polymers and mercury atom(s). The polymers (PANI, PES, and PAMAM) exhibit potential coordination

and binding sites characterised by high electron density, enabling them to bind positively charged ions and form complexes, as detailed in Section 4.3. In the instance of PAN1Hg, the mercury creates a bidentate complex with PANI, utilising both electron-rich aryl rings. The PANI binds with Hg ions using the C and H atoms, thus exhibiting a robust interaction between the two molecules. In a similar manner, bidentate complexation is observed in the PANI3Hg complex, which surrounds one aryl ring. Furthermore, two additional Hg ions were coordinated to the other aryl ring, resulting in the formation of monodentate complexes. PES1Hg demonstrated the establishment of a bidentate coordination at the electron-rich site of the molecule. PES3Hg exhibits tridentate complexation on one of the aromatic rings. In addition, each residual mercury ion is attached to the aromatic sulfone site of the molecule. PES interacts with Hg ions using its O, aromatic C and H skeleton. PAM1Hg exhibits a monodentate coordination with the C and N atoms, whereas PAM3Hg demonstrates a comparable coordination along with an additional tridentate coordination sphere. The coordination pattern observed across the different polymers indicates that Hg ions preferentially bind to the electron-rich site of the molecules, forming stable complexes. The coordination capability of the Hg ions with the polymers indicates that there is a close proximity between the ions and the polymers. Therefore, it can be anticipated that when the polymers function as adsorbents and are in close proximity to metallic contaminants in wastewater, Hg ions will be successfully adsorbed. Therefore, this interaction is expected to occur during the remediation of mercury in wastewater utilising polymers as adsorbent agents. The extent of coordination can vary with differences in the electronic and structural characteristics of the polymers. This will be clarified in the following section.

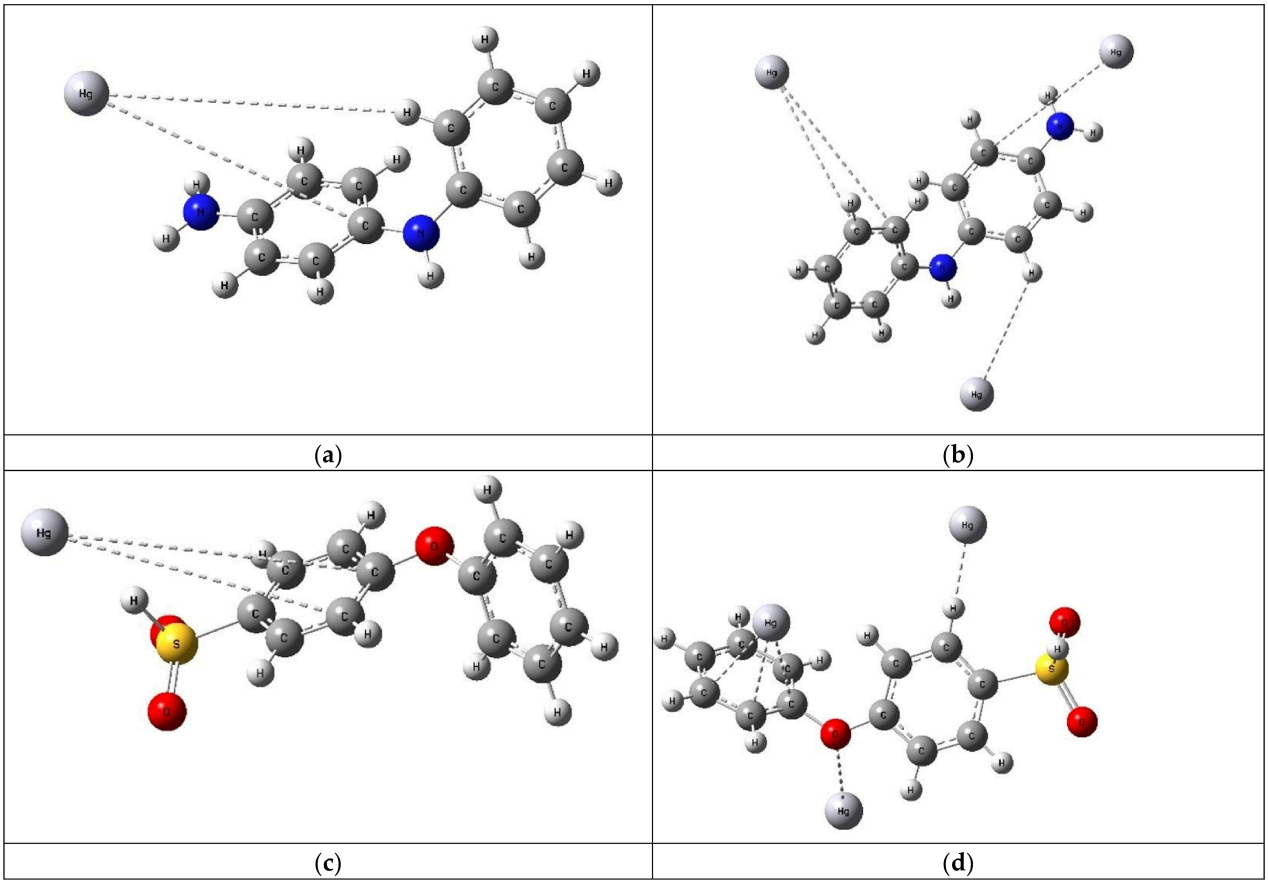

Figure 12. *Cont.*

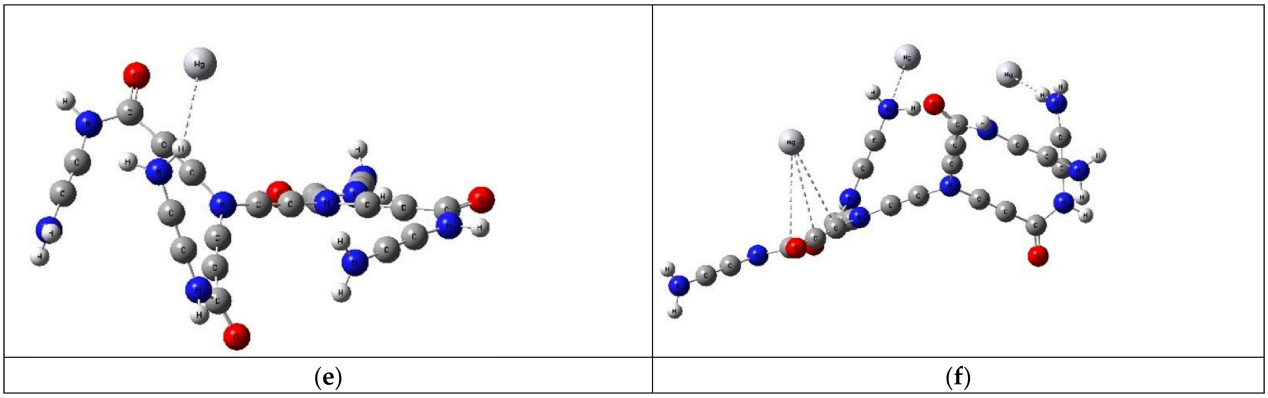

(**e**) (**f**)

Figure 12. Optimised complex molecules of (**a**) PAN1Hg, (**b**) PAN3Hg, (**c**) PES1Hg, (**d**) PES3Hg, (**e**) PAM1Hg and (**f**) PAM3Hg.

4.4.2. Binding Energies of Molecules After Interaction with Hg Atom(s)

The optimised structures of the PAN1Hg, PAN3Hg, PES1Hg, PES3Hg, PAM1Hg, and PAM3Hg complexes, along with their binding energies, are detailed in Table 3 to facilitate the analysis of molecular interactions. The binding energies ($E_{B.E}$) act as measures of the binding affinity between the polymer and mercury ions. A comparative analysis of binding energies for various complexes (single- and multi-mercury) was performed to identify which material shows greater potential for remediating mercury ions, thus reducing the concentration of dissolved mercuric contaminants in industrial effluents.

Table 3. Estimated binding energies of predicted complex molecules.

Complexes	PAN1Hg	PAN3Hg	PES1Hg	PES3Hg	PAM1Hg	PAM3Hg
$E_{B.E}$ (eV)	0.063	0.065	0.027	0.136	0.242	0.253
$E_{B.E}$ (kJ/mol)	6.04	6.30	2.63	13.13	23.37	24.42
E_F (eV)	−0.09565	−0.1008	−0.16045	−0.1453	−0.15055	−0.15055
E_g (eV)	0.1557	0.1452	0.1813	0.1564	0.1419	0.1367

PAMAM shows the maximum binding at low and high Hg^{2+} loading (PAM1Hg = 0.242 eV; PAM3Hg = 0.253 eV). The observed binding energy is consistent with the high density of nitrogen donors in PAMAM and its well-established role in the literature as a strong Hg^{2+} chelator via cooperative amine/amide coordination. The same magnitudes of PAM1Hg and PAM3Hg (ΔE = 0.011 eV) mean that the additional Hg^{2+} ions are hosted with a small additional stabilisation, consistent with a saturation-type binding behaviour at the multivalent arms of the dendrimer rather than a cooperative enhancement. For PANI, there is a little binding energy increase from single to triple Hg^{2+} loading (PAN1Hg = 0.063 eV to PAN3Hg = 0.065 eV) which shows that the aromatic backbone has little ability to stabilise multiple Hg^{2+} centres compared to PAMAM. The loading-dependent response exhibits a particularly prominent relative increase in PES for a five-fold increase in PES1Hg (0.027 eV) to PES3Hg (0.136 eV). This may indicate a cooperative or synergic contribution from the sulfone donor sites after the tridentate coordination is established through the aromatic ring system.

The measured energies (2.6–24.4 kJ mol^{-1}) are consistent with weak to moderate non-covalent interactions (e.g., strong hydrogen bonds or weak dative coordination) and do not suggest strong covalent Hg-N/Hg-O bond formation. This is important because it implies that the Hg^{2+} interaction is chemisorptive (as seen from the DOS hybridisation) but thermodynamically moderate rather than extremely strong. This is good for the adsorbent regeneration, as moderate binding strength allows easier desorption in acid-wash recovery

cycles than very high-energy irreversible binding. Therefore, it can be predicted that PES and PAMAM will successfully remove Hg from wastewater. A combination of two or three polymers will yield greater effectiveness in mercury remediation [51].

Concentration-dependent DFT studies of the binding energies for the adsorption of mercury (Hg^{2+}) show a consistent trend, with PAMAM found as the strongest binder in both single- and multi-ion loading. The most favourable interaction at single-Hg^{2+} loading is found for PAM1Hg (0.242 eV, 23.37 kJ mol^{-1}), followed by PAN1Hg (0.063 eV, 6.04 kJ mol^{-1}) and PES1Hg (0.027 eV, 2.63 kJ mol^{-1}). In the case of three-Hg^{2+} loading, PAMAM shows the maximum binding affinity with PAM3Hg (0.253 eV, 24.42 kJ/mol), followed by PES3Hg (0.136 eV, 13.13 kJ/mol) and PAN3Hg (0.065 eV, 6.30 kJ/mol). The measured data indicate that PAMAM has consistently shown a strong binding affinity, independent of Hg^{2+} loading, whereas PES shows the largest proportional increase in binding strength from single- to triple-ion coordination.

PAMAM exhibits good efficiency at low Hg^{2+} concentrations relevant to South African regulatory limits ($\leq$0.006 mg L^{-1} and <0.002 mg L^{-1}) through multidentate chelation, in agreement with the high single-ion binding affinity of PAM1Hg. For industrial wastewater treatment, PAMAM exhibits the highest overall binding affinity for Hg^{2+} among the three polymers, as evidenced by PAM3Hg at higher Hg^{2+} concentrations. This is achieved through the cooperative participation of terminal amine and interior amide donor sites in a multivalent, cage-like coordination sphere. PES shows an astonishingly strong secondary function at high loading with binding affinity by far increased from PES1Hg to PES3Hg. This suggests that Hg^{2+} concentration promotes the involvement of sulfone-rich domains. By comparison, PANI shows a lower energy gain for PAN1Hg vs PAN3Hg, indicating that although it is chemisorptively active through its aromatic backbone, it provides a smaller thermodynamic driving force for multi-ion capture than PAMAM and PES.

These results suggest that PAMAM is the most universally effective adsorbent for the concentration range studied and is appropriate for both polishing-stage treatment at trace levels close to regulatory discharge limits and higher-concentration industrial applications where the multidentate chelation chemistry of PAMAM dominates. The proportional increase in PES contribution at high Hg^{2+} levels suggests a secondary role for PES in the nanocomposite, enhancing the sulfone matrix's ability to stabilise additional binding sites as the ion concentration increases. On the other hand, the redox-active conjugated backbone of PANI largely offers electronic delocalisation and structural conductivity to the hybrid system, instead of being the main thermodynamic driving factor for adsorption. The analysis of the binding energy with respect to concentration provides a systematic and elegant way to experimental design. This highlights the need for coupling computational and experimental techniques for the adsorption study and suggests a nanocomposite approach. In this method, the structural properties of PES and the electrical properties of PANI enhance PAMAM's chelation capacity.

4.4.3. Density of States (DOS) of Polymer–Hg^{2+} Ion Interaction

The DOS profiles shown in Figure 13 indicate three substantial electronic effects of Hg^{2+} interaction with individual polymers, viz. changes in the Fermi level (E_F), narrowing of the energy gaps (E_g), and orbital hybridisation. The reference E_F values before Hg^{2+} coordination for polyaniline (PANI), polyethersulfone (PES) and poly(amidoamine) (PAMAM) are −0.096 eV, −0.1585 eV, and +0.1592 eV, respectively, and all of them suffer considerable alterations upon complex formation. Importantly, the positive E_F of PAMAM indicates the electron-rich and nitrogen-rich nature of PAMAM and is supported by the shortest computed HOMO–LUMO gap (E_g: PES > PANI > PAMAM) and the largest ΔN_{max} (2.49).

PAMAM demonstrates a considerable E_F change to −0.15055 eV (ΔIEF = −0.310 eV) upon coordination with Hg^{2+}, which is much bigger than that for PANI and PES. This downshift is a quantitative manifestation of the redistribution of electron density from the nitrogen donors of PAMAM to the unoccupied 6s/6p orbitals of Hg^{2+}, analogous to p-type doping. This is also supported by FTIR analysis. FTIR analysis shows the N-H and Amide I groups, which are important lone-pair donors which allow for significant charge transfer. The same E_F for PAMAM1Hg and PAMAM3Hg suggests saturation behaviour. The first Hg^{2+} ion balances the Fermi level, while subsequent ions are incorporated *via* multi-arm tridentate chelation without altering net charge transfer, as indicated by a plateau in the adsorption isotherm.

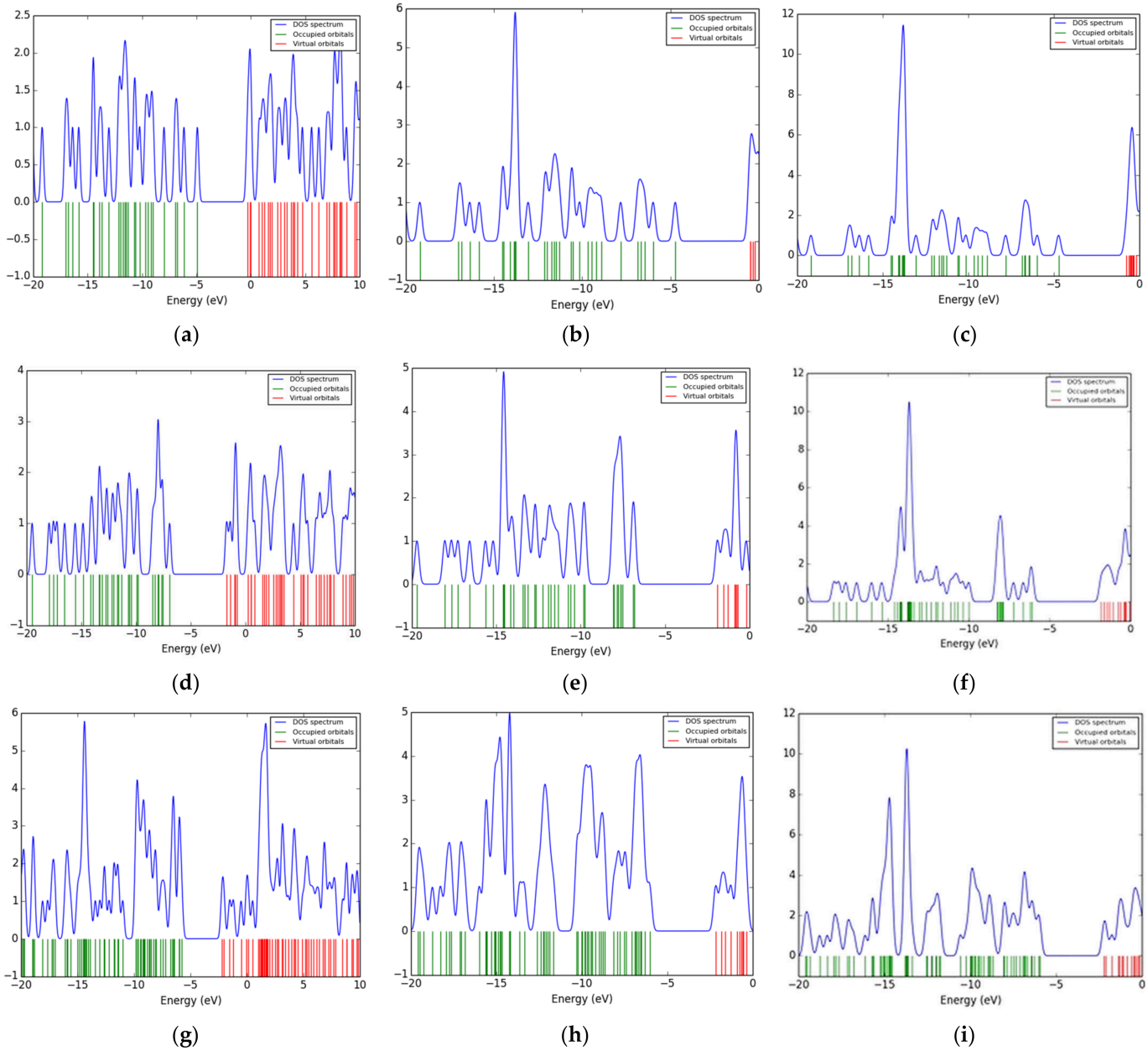

Figure 13. DOS plot of (**a**) PANI, (**b**) PANI1Hg, (**c**) PANI3Hg, (**d**) PES, (**e**)PES1Hg, (**f**) PES3Hg, (**g**) PAMAM, (**h**) PAMAM1Hg and (**i**) PAMAM3Hg.

Contrarily, PES exhibits a sign reversal in E_F shift, where PES1Hg exhibits a downshift (−0.00195 eV), and PES3Hg exhibits an upshift (+0.0132 eV), implying a complex mechanism where electron withdrawal at the aryl-ether site switches to partial back-donation

affected by the sulfone group at higher Hg^{2+} concentrations. DOS clarifies that this feature cannot be found through extensive HOMO–LUMO gap investigations.

All six polymer–Hg^{2+} complexes exhibit a decrease in E_g relative to their isolated counterparts. This phenomenon can be predicted from quantum mechanics: the coordination stabilises the LUMO of the complex, which has contributions from Hg 6s/6p orbitals, while the HOMO retains its polymeric N/O lone-pair character, lowering the energy gap. This reduction implies some experimentally observable consequences: (i) bathochromic shift in UV–Vis spectra of the adsorbed complexes, and (ii) increase in the electrical conductivity of the PANI upon Hg^{2+} loading, increasing the density of states (DOS) at E_F. This conclusion can be experimentally verified by four-probe conductivity measurements.

The complex density of states results in the emergence of new hybrid states not present in the isolated components. This discovery validates the chemisorptive nature of polymer–Hg^{2+} binding, involving genuine dative N $\rightarrow$ Hg^{2+} and O $\rightarrow$ Hg^{2+} orbital overlap, rather than just electrostatic attractions. In the FTIR results, the distinctive bands corresponding to the principal coordination sites undergo red shifts upon binding Hg^{2+}, consistent with the formation of dative bonds and indicative of reduced bond order. In conclusion, the DOS data provide an orbitally resolved approach to relate macroscopic characterisations (as detailed by FTIR, UV–Vis and SEM/EDX) to DFT-calculated binding energy hierarchies, validating the suitability of PAMAM for trace Hg^{2+} removal and PANI's efficiency in high-concentration situations.

5. Conclusions

By integrating density functional theory calculations with practical characterisation, this study explores the use of conductive polymers—polyaniline (PANI), polyethersulfone (PES), and polyamidoamine (PAMAM)—as adsorbents for mercury remediation in contaminated water. These polymers exhibit advantageous morphologies and functional groups for mercury adsorption, including porous surfaces and aromatic frameworks, as determined by structural analysis. By donating electrons, active groups such as amines and sulfones enhance the interaction between mercury ions, as indicated by spectroscopic investigations. According to computational modelling, PAMAM shows a strong affinity for mercury due to its small HOMO–LUMO gap, leading to high electrical reactivity. PANI is excellent at multiple ion contacts, whereas PAMAM can form stable complexes with mercury, as indicated by binding energy studies. Stability is increased by nitrogen and oxygen, which are rich in electrons and primarily aid in mercury binding. The results indicate that conductive polymers efficiently adsorb mercury via structural and electrical interactions, which can guide the development of sophisticated adsorbents and filtration membranes for water purification. Furthermore, in this study we have systematically identified the practical drawbacks of prepared materials for mercury removal and proposed feasible improvement strategies. For example, PANI is prone to oxidative degradation and low porosity. Hence, we suggest strategies such as modification of the composites with sulphur-rich or amine ligands and physicochemical optimisation of the processes to increase porosity and hydrophilicity. It is hoped that these strategies bridge the theoretical understanding and engineering applications, paving the way for future studies towards scalable, regenerable and high-performance polymer adsorbents for mercury remediation. In the end, this research supports the development of sustainable technologies for treating contaminated water by highlighting the potential of hybrid systems combining various polymers to enhance remediation efficiency.

Author Contributions: Conceptualization, N.F., U.P. and A.O.; methodology, H.S., S.Z. and S.M., software, H.S. and S.M.; validation, N.F., U.P. and A.O.; formal analysis, H.S., S.Z. and S.M.; investigation, H.S., S.Z. and S.M.; resources, H.S., S.Z., N.F., U.P. and S.M.; data curation, S.M. and H.S.; writing—original draft preparation, H.S. and S.M.; writing—review and editing, N.F., U.P., S.Z. and A.O.; supervision, H.S., A.O. and N.F.; project administration, N.F.; funding acquisition, N.F. All authors have read and agreed to the published version of the manuscript.

Funding: This research was jointly funded by the Research and Innovation office of the iYunivesithi Walter Sisulu, Mthatha, South Africa, and the Tertiary Education Support Program (TESP), Eskom Holding SOC Limited, South Africa, Reg No: 2002/015527/0. While the APC was funded by the iYunivesithi Walter Sisulu, Mthatha, South Africa.

Data Availability Statement: The original contributions presented in this study are included in the article. Further inquiries can be directed to the corresponding authors.

Acknowledgments: S.M., H.S. and N.F. are grateful to iYunivesithi Walter Sisulufor providing computational resources, postdoctoral funding and the APC. S.M. and N.F. appreciate the Tertiary Education Support Program (TESP), Eskom Holding SOC Limited and Long-Term European Union-African Union Research and Innovation Partnership on Renewable Energy (LEAP-RE), for providing a postgraduate bursary. S.M., H.S. and N.F. appreciate Raymond Taziwa for proofreading and Uliana Pinaeva for instrumental analysis.

Conflicts of Interest: The authors declare no conflicts of interest.

References

1. Qasem, N.A.; Mohammed, R.H.; Lawal, D.U. Removal of heavy metal ions from wastewater: A comprehensive and critical review. *npj Clean. Water* **2021**, *4*, 36. [CrossRef]
2. Hasheesh, M.; El-Kashif, E.F.; Mohamed, A.; Saood, M. The effect of activated carbon nanoparticles (ACNPs) on characterization and mechanical properties of polyethersulfone (PES) ultrafiltration membranes. *Polym. Bull.* **2024**, *81*, 14855–14874. [CrossRef]
3. Tajik, S.; Beitollahi, H.; Nejad, F.G.; Dourandish, Z.; Khalilzadeh, M.A.; Jang, H.W.; Venditti, R.A.; Varma, R.S.; Shokouhimehr, M. Recent developments in polymer nanocomposite-based electrochemical sensors for detecting environmental pollutants. *Ind. Eng. Chem. Res.* **2021**, *60*, 1112–1136. [CrossRef] [PubMed]
4. Amico, D.; Tassone, A.; Pirrone, N.; Sprovieri, F.; Naccarato, A. Recent applications and novel strategies for mercury determination in environmental samples using microextraction-based approaches: A review. *J. Hazard. Mater.* **2022**, *433*, 128823. [CrossRef] [PubMed]
5. Pavithra, K.G.; SundarRajan, P.; Kumar, P.S.; Rangasamy, G. Mercury sources, contaminations, mercury cycle, detection and treatment techniques: A review. *Chemosphere* **2023**, *312*, 137314. [CrossRef] [PubMed]
6. Narouei, F.H.; Livernois, L.; Andreescu, D.; Andreescu, S. Highly sensitive mercury detection using electroactive gold-decorated polymer nanofibers. *Sens. Actuators B Chem.* **2021**, *329*, 129267. [CrossRef]
7. Umataliyevna, U.K.; Bobojonov, K.S.; Asanaliyevna, S.Z.; Muxsimovna, A.M.; Mamadjanovna, T.F.; Shavkatovna, A.M.; G'ulom o'gli, A.U.B.; Abdujalol o'g'li, G.A. Priority toxic metals arsenic, cadmium, mercury, and lead in ecosystems: A review of sources, toxicity, and regulatory approaches. *Chem. Rev. Lett.* **2025**, *8*, 883–902.
8. Zhumanazar, N.; Korolkov, I.V.; Yeszhanov, A.B.; Shlimas, D.I.; Zdorovets, M.V. Electrochemical detection of lead and cadmium ions in water by sensors based on modified track-etched membranes. *Sens. Actuators A Phys.* **2023**, *354*, 114094. [CrossRef]
9. Mustafa, Z.; Ghadai, R.K.; Pradhan, B.; Swain, B.P.; Biswas, J.; Kumar, D. Recent advances in polyaniline/graphene nanocomposites for supercapacitor applications: Synthesis, properties, and future directions. *Results Surf. Interfaces* **2024**, *17*, 100316. [CrossRef]
10. Rezaee, D.; Esfandian, H. Innovative NiO/PANI nanocomposite derived from Ni-MOF for enhanced supercapattery electrode performance. *Results Chem.* **2025**, *17*, 102543. [CrossRef]
11. Diggikar, R.S.; Deshmukh, S.P.; Thopate, T.S.; Kshirsagar, S.R. Performance of polyaniline nanofibers (PANI NFs) as PANI NFs-silver (Ag) nanocomposites (NCs) for energy storage and antibacterial applications. *ACS Omega* **2019**, *4*, 5741–5749. [CrossRef]
12. Yadav, A.K.; Mohammad, N.; Chamanehpour, E.; Mishra, Y.K.; Khanna, P.K. Polyaniline (PANI) nanocomposites with Se, Te and their metal chalcogenides: A review. *RSC Appl. Polym.* **2024**, *2*, 775–794. [CrossRef]
13. Khattak, S.G.; Safi, M.A.; Shah, M.; Aziz, A.; Muhammad, Y.; Hassan, H.; Seema, H. Highly Sensitive and Selective PANI/Ag Nanocomposites-Based Gas Sensors for Room-Temperature NH3 Detection. *J. Mater. Appl.* **2025**, *14*, 1–13. [CrossRef]

14. Motlokoa, T.R.; Maboya, W.K.; Mbileni-Morema, C.; Modise, S.J.; Okoli, B.J. Modification of polyethersulfone with partially reduced graphene oxide and its water purification application. *Desalin. Water Treat.* **2025**, *323*, 101341. [CrossRef]
15. Heidari, Y.; Noroozian, E.; Maghsoudi, S. Electrospun nanofibers of cellulose acetate/metal organic framework-third generation PAMAM dendrimer for the removal of methylene blue from aqueous media. *Sci. Rep.* **2023**, *13*, 4924. [CrossRef] [PubMed]
16. Koeini, F.; Solouk, A.; Akbari, S. Graphene oxide-incorporated polylactic acid/polyamidoamine dendrimer electroconductive nanocomposite as a promising scaffold for guided tissue regeneration. *Macromol. Mater. Eng.* **2024**, *309*, 2400100. [CrossRef]
17. Bhadra, J.; Popelka, A.; Abdulkareem, A.; Ahmad, Z.; Touati, F.; Al-Thani, N. Fabrication of polyaniline–graphene/polystyrene nanocomposites for flexible gas sensors. *RSC Adv.* **2019**, *9*, 12496–12506. [CrossRef] [PubMed]
18. Al-Gamal, A.G.; Gado, W.S.; Abo El-Khair, M.A.; Zakaria, K.; Ragab, A.; Kabel, K.I. ZnO doped PAMAM for asphalt improvement as anti-corrosive coatings. *Sci. Rep.* **2024**, *14*, 28352. [CrossRef] [PubMed]
19. Cui, X.; Wu, M.; Liu, X.; He, B.; Zhu, Y.; Jiang, Y.; Yang, Y. Engineering organic polymers as emerging sustainable materials for powerful electrocatalysts. *Chem. Soc. Rev.* **2024**, *53*, 1447–1494. [CrossRef] [PubMed]
20. Poddar, A.K.; Patel, S.S.; Patel, H.D. Synthesis, characterization and applications of conductive polymers: A brief review. *Polym. Adv. Technol.* **2021**, *32*, 4616–4641. [CrossRef]
21. Zahran, M. Conducting dyes as electro-active monomers and polymers for detecting analytes in biological and environmental samples. *Heliyon* **2023**, *9*, e19943. [CrossRef] [PubMed]
22. Ganachari, S.V.; Shilar, F.A.; Patil, V.B.; Khan, T.Y.; Saleel, C.A.; Ali, M.A. Optimizing ammonia detection with a polyaniline–magnesia nano composite. *Polymers* **2024**, *16*, 2892. [CrossRef] [PubMed]
23. Le, Q.H.; Smida, K.; Abdelmalek, Z.; Tlili, I. Removal of heavy metals by polymers from wastewater in the industry: A molecular dynamics approach. *Eng. Anal. Bound. Elem.* **2023**, *155*, 1035–1042. [CrossRef]
24. Santos, T.J.; Paggiaro, J.; Pimentel, H.D.C.S.; dos Santos Pereira, A.K.; Cavallini, G.S.; Pereira, D.H. Computational study of the interaction of heavy metal ions, Cd (II), Hg (II), and Pb (II) on lignin matrices. *J. Mol. Graph. Model.* **2022**, *111*, 108080. [CrossRef] [PubMed]
25. Raji, Z.; Karim, A.; Karam, A.; Khalloufi, S. Adsorption of heavy metals: Mechanisms, kinetics, and applications of various adsorbents in wastewater remediation—A review. *Waste* **2023**, *1*, 775–805. [CrossRef]
26. Bihain, M.F.R.; Gomes, E.J.C.M.; Macedo, V.S.; Cavallini, G.S.; Pereira, D.H. Theoretical insights into the possibility of removing CH3Hg+ using different adsorptive matrices: G-C3N4, cellulose xanthate, and vanillin-derived modified monomer. *J. Mol. Liq.* **2022**, *361*, 119691. [CrossRef]
27. Lan, Y.; Xu, S.; Fu, Y.; Jin, L.; Han, Y.; He, X.; Wang, Q.; Lv, Y.; Cui, H. The selective adsorption mechanism of heteroatom-doped carbon nanotubes for heavy metals in wastewater. A DFT study. *Diam. Relat. Mater.* **2025**, *152*, 111875. [CrossRef]
28. Mokole, S.J.; Aliyu, A.; Fayemi, O.E. Electrochemical detection of dopamine using green and chemical synthesized CuO/PANI nanocomposite modified electrode. *Appl. Phys. A* **2023**, *129*, 148. [CrossRef]
29. Nagane, S.S.; Kuhire, S.S.; Mane, S.R.; Wadgaonkar, P.P. Partially bio-based aromatic poly (ether sulfone) s bearing pendant furyl groups: Synthesis, characterization and thermo-reversible cross-linking with a bismaleimide. *Polym. Chem.* **2019**, *10*, 1089–1098. [CrossRef]
30. Lyu, Z.; Ding, L.; Huang, A.-T.; Kao, C.-L.; Peng, L. Poly (amidoamine) dendrimers: Covalent and supramolecular synthesis. *Mater. Today Chem.* **2019**, *13*, 34–48. [CrossRef]
31. Lewis, D.F. Frontier orbitals in chemical and biological activity: Quantitative relationships and mechanistic implications. *Drug Metab. Rev.* **1999**, *31*, 755–816. [CrossRef] [PubMed]
32. Dhonnar, S.L.; Sadgir, N.V.; Adole, V.A.; Jagdale, B.S. Molecular structure, FT-IR spectra, MEP and HOMO-LUMO investigation of 2-(4-fluorophenyl)-5-phenyl-1, 3, 4-oxadiazole using DFT theory calculations. *Adv. J. Chem. Sect. A* **2021**, *4*, 220–230. [CrossRef]
33. Zheng, G.; Sonnenberg, L.; Hada, M.; Ehara, M.; Toyota, K.; Fukuda, R.; Hasegawa, J.; Ishida, M.; Nakajima, T.; Honda, Y. *Gaussian 09*; Gaussian Inc.: Wallingford, CT, USA, 2009; p. 48.
34. Gartner, T.E., III; Jayaraman, A. Modeling and simulations of polymers: A roadmap. *Macromolecules* **2019**, *52*, 755–786. [CrossRef]
35. Gao, P.; Jiang, X.; Li, J.; Nicolas, J.; Ha-Duong, T. Molecular simulations of polymer-based drug nanocarriers: From physical and structural properties to controlled release. *Adv. Healthc. Mater.* **2026**, *15*, e03503. [CrossRef] [PubMed]
36. Aslanova, H.; Shikhverdiyeva, N.; Seyidova, C.M.; Shikhverdiyev, I.; Tagiyev, S.D.; Zeynalov, N.; Tagiyev, D. Computational Strategies for Design and Optimization of Polymer-Supported Heterogenized Nanocatalysts. *J. Comput. Chem.* **2026**, *47*, e70383. [CrossRef] [PubMed]
37. Alamos-Musre, S.; Beltrán-Chacana, D.; Moyano, J.; Márquez-Miranda, V.; Duarte, Y.; Miranda-Rojas, S.; Olguín, Y.; Fuentes, J.A.; González-Nilo, D.; Otero, M.C. From structure to function: The promise of PAMAM dendrimers in biomedical applications. *Pharmaceutics* **2025**, *17*, 927. [CrossRef]
38. Anggraini, C.S.; Wahyuningrum, D.; Alni, A. The Synthesis of Polyethersulfone (PES) and its Derivatives as Polymer Light Emitting Diode (PLED) Material. *Key Eng. Mater.* **2019**, *811*, 126–132. [CrossRef]

39. Singh, L.; Singh, V. Synthesis of Ag@ PANI nanocomposites by complexation method and their application as label-free chemoprobe for detection of mercury ions. *J. Polym. Eng.* **2020**, *40*, 657–665. [CrossRef]
40. Gunes-Durak, S.; Acarer-Arat, S.; Tufekci, M.; Pir, İ.; Ustkaya, Z.; Oz, N.; Tufekci, N. Mechanical enhancement and water treatment efficiency of nanocomposite PES membranes: A study on Akçay dam water filtration application. *ACS Omega* **2024**, *9*, 31556–31568. [CrossRef] [PubMed]
41. Zhao, C.; Xue, J.; Ran, F.; Sun, S. Modification of polyethersulfone membranes–A review of methods. *Prog. Mater. Sci.* **2013**, *58*, 76–150. [CrossRef]
42. Yasir, A.T.; Benamor, A.; Hawari, A.H. Enhancement of polysulfone ultrafiltration membrane with third generation poly (amido amine)-graphene oxide nanocomposite. *J. Water Process Eng.* **2023**, *54*, 103991. [CrossRef]
43. Ban, G.; Long, J.; Yan, K.; Li, Q.; Huang, X.; Wei, X.; Xie, F. A new nanocomposite for inducing demineralized dentin remineralization. *Int. J. Nanomed.* **2025**, *20*, 1335–1349. [CrossRef] [PubMed]
44. Fayemi, O.E.; Letsholo, P.B.; Shoyiga, H.O.; Ahia, C.C.; Meyer, E.L. Investigation of the effects of concentration and voltage on the physicochemical properties of Nylon 6 nanofiber membrane. *Sci. Rep.* **2025**, *15*, 10865. [CrossRef] [PubMed]
45. Abd Ali, L.I.; Alesary, H.F.; Ismail, H.K.; Hassan, W.H.; Kareem, A.A.; Nile, B.K. Polypyrrole-coated zinc/nickel oxide nanocomposites as adsorbents for enhanced removal of Pb (II) in aqueous solution and wastewater: An isothermal, kinetic, and thermodynamic study. *J. Water Process Eng.* **2024**, *64*, 105589. [CrossRef]
46. Van Krevelen, D.W.; Te Nijenhuis, K. *Properties of Polymers: Their Correlation with Chemical Structure; Their Numerical Estimation and Prediction from Additive Group Contributions*; Elsevier: Amsterdam, The Netherlands, 2009.
47. Safi, B.; Balawender, R.; Geerlings, P. Solvent effect on electronegativity, hardness, condensed Fukui functions, and softness, in a large series of diatomic and small polyatomic molecules: Use of the EFP model. *J. Phys. Chem. A* **2001**, *105*, 11102–11109. [CrossRef]
48. Gajalakshmi, D.; Tamilmani, V. Tuning pyrrole oligomers for optoelectronic and anti-corrosion applications: A DFT/TDDFT study. *Theor. Chem. Acc.* **2020**, *139*, 175. [CrossRef]
49. Koparir, P.; Omar, R.A.; Sarac, K.; Ahmed, L.O.; Karatepe, A.; Taskin-Tok, T.; Safin, D.A. Synthesis, characterization and computational analysis of thiophene-2, 5-diylbis ((3-mesityl-3-methylcyclobutyl) methanone). *Polycycl. Aromat. Compd.* **2023**, *43*, 6107–6125.
50. Omar, R.A.; Koparir, P.; Sarac, K.; Koparir, M.; Safin, D.A. A novel coumarin-triazole-thiophene hybrid: Synthesis, characterization, ADMET prediction, molecular docking and molecular dynamics studies with a series of SARS-CoV-2 proteins. *J. Chem. Sci.* **2023**, *135*, 6. [CrossRef] [PubMed]
51. Camarada, M.; Zúñiga, M.; Alzate-Morales, J.; Santos, L. Computational study of the complexation of metals ions with poly (amidoamine) PAMAM G0 dendrimers. *Chem. Phys. Lett.* **2014**, *616*, 171–177. [CrossRef]